國立交通大學

光電工程研究所
碩士論文

埋入菱形溝槽內之光纖透鏡模組 與
直立式相位型微光柵

Fiberlens in the rhombus-shaped channel and

Free-space phase microgratings

研究生：黃翌軒

指導教授：謝漢萍 教授

中華民國九十三年七月

埋入菱形溝槽內之光纖透鏡模組 與
直立式相位型微光柵

Fiberlens in the rhombus-shaped channel and

Free-space phase microgratings

研 究 生：黃翊軒 　　　　Student：Yi-Husan Huang

指導教授：謝漢萍 教授 　　Advisor：Dr. Han-Ping D. Shieh

國 立 交 通 大 學

光 電 工 程 研 究 所

碩 士 論 文

A Thesis
Submitted to Institute of Electro-Optical Engineering
College of Electrical Engineering and Computer Science
National Chiao Tung University
In Partial Fulfillment of the Requirements
For the degree of
Master
In
Electro-Optical Engineering

July 2004

Hsin-Chu, Taiwan, Republic of China

中華民國九十三年七月

埋入菱形溝槽內之光纖透鏡模組 與
直立式相位型微光柵

碩士研究生：黃翊軒　　　指導教授：謝漢萍 教授

國立交通大學 光電工程研究所

中文摘要

因應信息處理的蓬勃發展，快速的資訊存取時間、小型化的伺服系統以及高儲存密度成為光儲存科技發展的指標。為了縮減光學讀寫頭的尺寸與重量，目前已有多種微型光學系統已被提出，然而幾乎都有著光效率不佳的問題。既然光資訊儲存密度取決於雷射光源的波長，以藍光雷射（405nm 波段）為光源的微型光學系統將逐漸被應用於光學讀寫頭上。

在現有的微型光學讀寫頭系統中，雷射光源通常建構於系統內，但是由於雷射光源所散發的廢熱甚少佚失至外界，易於發生廢熱積聚的現象，使得雷射光源的壽命因而減低，此外光學系統的光軸高度幾乎完全取決於雷射二極體活動層的高度，因此提出埋入菱形溝槽內的光纖透鏡模組，利用光纖透鏡模組將光束有效地導入讀寫頭系統中，如此雷射二極體便可從系統中分離出來，廢熱也因此能有效地被佚失至系統之外，加上菱形溝槽適於光纖精確定位與光軸高度的控制，廢熱積聚與光軸調制的問題便可獲得解決，並且可藉由光纖透鏡提供近似圓形的光

束及縮小邊射型雷射光源的發散角，而達到光束整形的功效。

　　在現有的自由空間型微型光學讀寫頭中，微型光柵的成分為多晶矽，但是藍光對多晶矽的穿透性不高，因此系統的光學效率極低，於是我們設計一個在藍光波段具有高穿透效率的三維微光柵以作為光學讀取頭的關鍵元件，其光柵部份由對藍光波段具高穿透性的Si_3N_4構成，並由光學軟體G-SOLVER 估算出光柵厚度約為 0.75um可在較大製程公差的情況下取得合適的繞射效率分佈（0 階與+1 或 -1 階繞射光束的光效率比值約為 6～12）。根據前述的設計，將此三維微型光柵利用微光機電製程來實現，並從此微型光柵之繞射光束的量測結果得到光效率比值約為 5，藉由提升微型矩形光柵的製程品質來減輕梯形化現象，則此光效率分佈的誤差即可獲得改善。
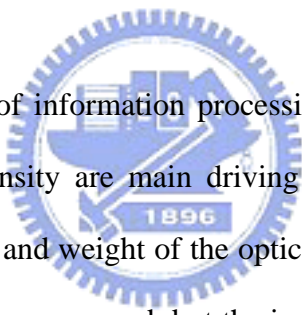
Fiberlens in the rhombus-shaped channel and Free-space phase microgratings

Student：Yi-Husan Huang   Advisor：Dr. Han-Ping D. Shieh

Institude of Electro-Optical Engineering

National Chiao Tung University

Abstract

With the rapid progress of information processing, fast access time, small-size drives and high recording density are main driving factors of optical data-storage techniques. To reduce the size and weight of the optical pickup-head, several kinds of micro-optical systems have been proposed, but the issue of low light efficiency exists in those systems. Since the storage density is determined by the wavelength of laser, the blue-laser (405 nm) will be widely adopted as the light source of the micro optical pickup-head system.

At present, the laser sources are placed in the pickup-head system. Since the heat dissipation rate of the laser diode is quite slow, thermal accumulation decreases the lifetime of laser diode. Besides, the optical axis height is constrained by the active layer of the laser diode. To solve these issues, the module with a fiberlens inserted in the rhombus-shaped channel is proposed. With this module, the beam is guided into the pickup-head, so the laser diode can be separated from this system. Since the laser

diode is outside the pickup-head, the heat can be dissipated efficiently. Besides, the rhombus-shaped channel is suitable for the fiber-alignment and the control of optical axis height. Therefore, the issues of thermal accumulation and limited optical axis height are improved. Additionally, as a beam-shaping component, the fiberlens yields a more circularly-shaped incident beam with small divergence angles.

In the free-space micro pickup-head system proposed by M. C. Wu, the micro-grating is made of the poly-silicon. However, the poly-silicon is nearly opaque in the blue-laser spectrum, so the light-efficiency is quite low. Therefore, we designed a novel 3-dimensional micro-grating as one of key components in the pickup-head. The ridges of microgratings are made of the Si_3N_4, since the blue-laser is transmissible through the Si_3N_4 layer. Diffraction efficiency distribution of microgratings is suitable for the pickup-head (the diffraction efficiency ratio is from 6 to 12 between 0 and +1 or -1 orders), when grating thickness is 0.75um according to the simulated results of G-SOLVER software. According to this design, the 3-dimensional micrograting was realized by the MOEMS process. Finally, measurement results of the three-beamed microgratings showed that the diffraction efficiency ratio is 5, while the deviation of diffraction efficiency distribution might be reduced by trimming the profile of microgratings from trapezoid to rectangular shape.

誌　　謝

Table of Contents

Abstract (Chinese)

Abstract (English)

Acknowledgments

Table of Contents

List of Tables

Figure Caption

Figure caption

List of tables

Chapter 1

Introduction

1.1 Introduction

With the tremendous improvement on the processes of semiconductor electronics, micro-opto-electric-mechanical-system (MOEMS) technology opens up many new opportunities for optical and optoelectronic applications, and offers unprecedented capabilities in extending the functionality of optical devices and the miniaturization of optical systems.

Compared with the conventional optical systems, the micro-optics, of which dimension is 0.01mm to 1mm, provides optical systems with positioning all elements precisely by the photolithography, assembly and packaging. Therefore, the micro -optical systems not only avoid complex optical-path alignment and improve the optical stability, but also incorporate other systems conveniently. The integration scheme can be extended to include electronic control and sensing circuits by combining the micromachining process with standard VLSI processing. Movable structures, micro-actuators, micro-sensors, and micro-optical elements such as microgratings can be integrated on the same substrate by using batch processing technology.

At present, the development of micro-optics mainly progresses in the microscopy and integrated optical systems. The former is utilized in the Bio-photonics [1] [2], and the latter is applied to the pickup-head, the display such as the DMD (Digital Mirror

Device proposed by Texas Instruments) [3], 2D projectors and fiber communication.

The increasing processing speed of computers also promotes the requirement for mass storage systems with growing capacities and data access rate. To increase the storage capacity per unit area, it is possible either to increase the storage density or to use larger areas for data storage. However, a large storing area results in long scanning distances of the optical pickup-heads and slow access time. Since the storage density is determined by the wavelength of laser, the blue-laser (405 nm) is gradually adopted in high-density storage system to increase data capacity.

The optical pickup-head is used to read or write digital information onto the optical disk, and is comprised of several optical elements such as a laser diode, a diffractive grating, a reflective mirror, an objective lens and a photodiode, etc., whereas these optical elements can be constructed and integrated by MOEMS processes. Integration of the pickup head on a single substrate not only significantly reduces the expensive assembly processes of bulk optical components, but also greatly increases the data access rate, a feature particularly demanding for the computer and multimedia applications. Since the pickup-heads are placed on the actuators controlled by feedback loops, lighter heads allow the actuators to move at higher rate but with higher reliability of tracking. Generally, the resonance frequency (f) or data access rate of the actuator is determined by the equation 1-1, where m and k denote the weight and the elasticity of movable mechanisms, respectively.

$$f = \sqrt{\frac{k}{m}}$$ Eq.1-1

Therefore, the wide-bandwidth servo-system can be achieved by lightening the pickup head located on the actuator.

Recently, great efforts have been made to miniaturize and integrate the optical pickup-heads. Optical micro-pickup-heads are examples for the realization of integrated micro-optics. Undoubtedly, the slim and fine drives for CD-ROM or DVD-ROM players will be realized in the near future.

1.2 The development of miniaturized pickup-head

Integrated optics has been an active research area since it was proposed [4]. Most of the research efforts in integrated optics have been on guided wave systems. However, free-space optics offers many unique advantages that can not be achieved in guided wave devices. For example, free-space optics allows three-dimensional optical interconnections that could significantly improve the communication bottlenecks in very large semiconductor integrated systems. Much higher spatial bandwidth can also be achieved in free-space optics as opposed to guided wave devices. It is also possible to perform sophisticated optical information processing, such as Fourier transforms, in a free-space system using lenses.

However, most of the present free-space optical systems are comprised of bulk optical elements or multiple plane micro-lens arrays that can not be integrated on a single chip. They are, instead, discrete microsystems. Micromachining of silicon substrate has been applied to miniature optical bench and integrated optical systems since the 1970's [5].

Micromachining allows an inexpensive and reproducible batch processing of optical components. However, to date, most of the micro-optical components and systems are designed for optical access normal to the substrate surface because the microfabricated optical elements are confined to and within the surface of the substrate [6] [7]. Since external optics is needed for optical systems using components restricted within the substrate surface, monolithic integration of complete optical system on a single chip is not possible by these technologies.

Monolithic integration of a whole optical system or a micro-optical system, drastically reduces its size, weight and cost. Furthermore, expensive packaging process of individual optical components is possibly eliminated. One key component for a monolithic micro-optical system is an out-of-plane optical element, an optical element which is not confined to the surface of the substrate. In particular, vertical optical components standing perpendicularly to the surface allow multiple elements to be cascaded along the optical axis on the substrate. The LIGA (Lithographie Galvanofoemug Abformung) process can produce tall structures with a height of several hundred micrometers and can be used to fabricate optical elements, although X-ray lithography is required to do so. However, it is very difficult to create patterns such as lenses or gratings on the sidewalls of the tall structures fabricated by LIGA.

Recently, a micro-hinged technology has been developed which allows three-dimensional structures to be assembled from thin plates on the surface of the substrate [8]. The technology is based on surface micromachining and is compatible with most micro-actuator fabrication processes. Using surface micromachining, integrated micro-optical elements can be patterned by conventional photolithography and etching techniques and then made to stand perpendicularly on the same substrate.

The substrate serves as a micro-optical bench, so that lenses, mirrors and other components are prealigned by photolithography. Therefore, free-space structures present promising opportunities for the fabrication of optical systems.

1.2.1 Planar micro-pickup-heads

T. Shiono *et al* [9] integrated various planar diffractive structures on one single substrate for realizing micro-optical systems. The substrate may either be glass, plastic or silicon, provided it is transparent at the wavelength used. The substrate is used as the light guide in which the beam propagates along a zig-zag optical path, as shown in Fig. 1-1. Surface-mount optoelectronic components on the substrate surfaces are employed for handling, cooling, testing, and repair purposes. In this system, the beam sequentially hits those diffractive elements coated with reflective layers. Firstly, a reflective feedback lens is used for coupling a portion of the light back into the laser diode for stabilizing the resonator and avoiding wavelength variations. Then, through the collimation and beam-splitting, a transmissible and off-axis diffractive lens focuses the beam onto the disk. Finally, the beam is focused on the photodiode in the backward path, and the focusing and tracking error detections are based on the Foucault and push-pull methods, respectively. The focused spot size is about 1.0 μm at λ = 0.63 μm. This value is close to the diffraction limit (0.98 μm). Theoretical efficiency of the system is about 46 %, with reflection loss neglected at each interface.

However, the diffractive planar micro-optics is susceptible to high coupling loss of the laser diode. High optical crosstalk also exists in this system, because the high order diffracted beams become a source of crosstalk since light is confined to the slab. Beside, the aberration of this system is serious since its optical path is asymmetrical.
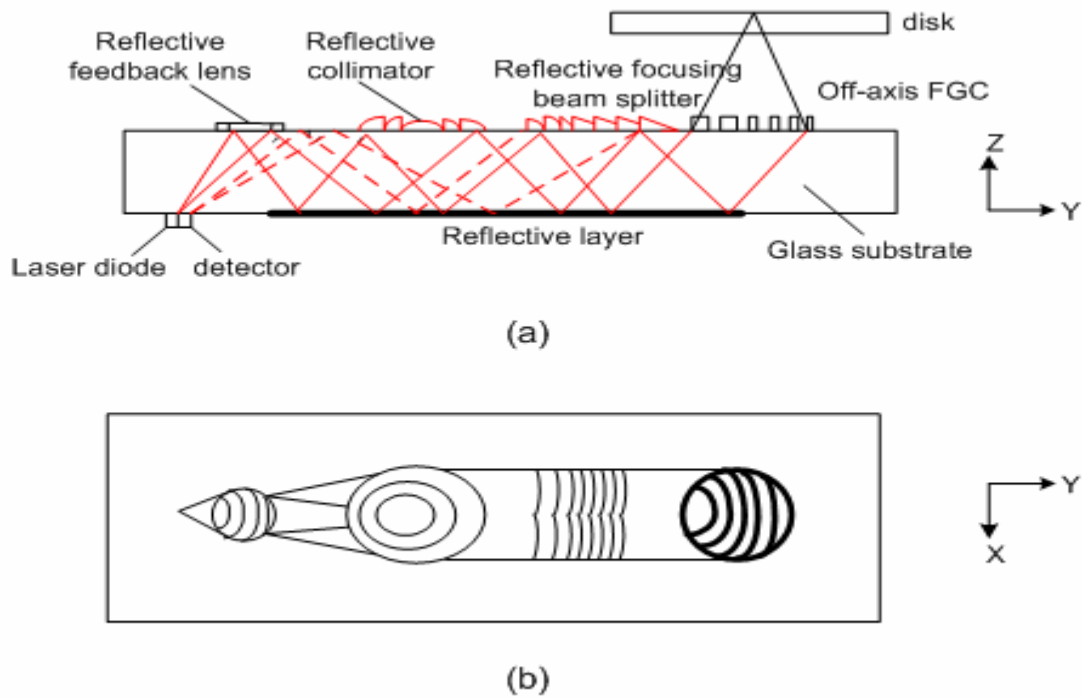
Fig. 1-1 Schematic of the planar optical pickup head based on the glass-substrate (a) side, and (b) top view.

1.2.2 Stacked micro-pickup-heads

The term stacked optics was coined by Iga et al. in 1982 [10]. Using 2D arrays of optical components separately fabricated on substrates to build integrated imaging systems, the alignment task of parallel optical systems is reduced to the alignment of the 2D component arrays rather than the individual components. The systems are arranged such that each planar substrate only contains one type of optical elements. In stacked optics, a variety of different substrates can be used in the system. Therefore, it is possible to use optimized techniques to fabricate each class of components. For example, the microlenses fabricated in glass substrates can be integrated with microgratings fabricated in photoresist substrates. However, the different behavior of the substrates may cause the difficulty of bonding under changing environmental

conditions (e.g., different thermal expansion coefficients).

These optical components such as a grating and hologram optical element can be achieved by dry etching and bonded sequentially as shown in Fig. 1-2. The depth of each element representing the thickness of wafer is equal to 500um, so this stacked pickup head is about 3mm in thickness. These optical elements are respectively fabricated on different silicon wafers with Si_3N_4 membranes. The holographic optical element (HOE) is the key component in this system, and it has the function of beam-deflecting and astigmatism for the focusing error detection.

The yield and optical performance of this system are high. However, since holographic optical elements (HOE) are dispersive elements, the deviation of wavelength is an issue in this optical design. Besides, it is difficult to precisely bond several chips. Critically, this system can not integrate with the actuators, so it encounters serious problems about dynamical tracking and focusing [11].
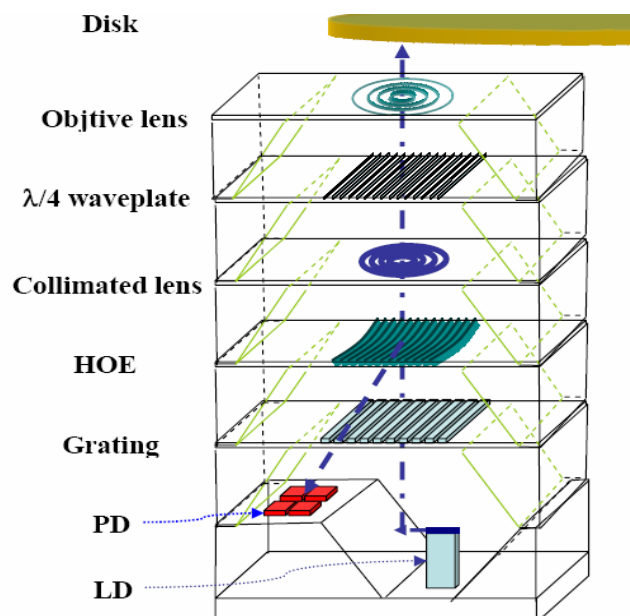
Fig. 1-2. Schematic of the stacked diffractive pickup head [11]

1.2.3 Free-space three-dimensional micro-pickup-heads

As proposed by M. C. Wu *et al*. [12], this optical pickup-head was also used to read and to write data from the optical disk, and was fabricated with the micro-optical bench technology [13] [14]. The schematic configuration based on the free-space micro-optical bench is shown in Fig. 1-3. This system includes a passively self-aligned semiconductor laser, and a variety of surface-micromachined micro-optical elements such as a collimating Fresnel-lens, a rotatable beam-splitter, a focusing Fresnel-lens, an inclined micro-mirror, and an integrated photodetector. These elements are out of plane, and mounted on top surface of the substrate. Three-dimensional passive optical elements, such as lenses, mirrors, gratings and beam-splitters, and active optical electrical components, such as photodiodes, are fabricated monolithically on a chip within an area of approximately a few millimeters square. Light from the laser diode propagates in free-space between these optical elements.
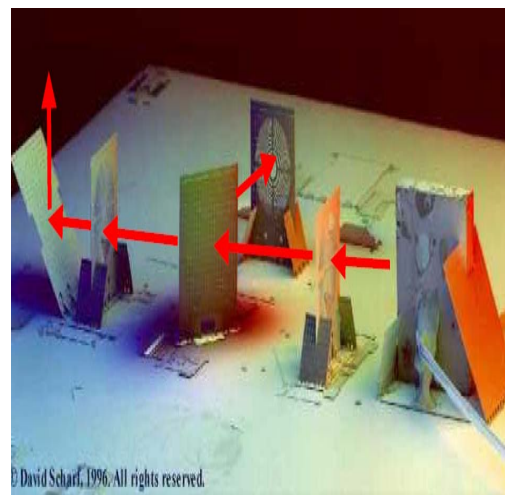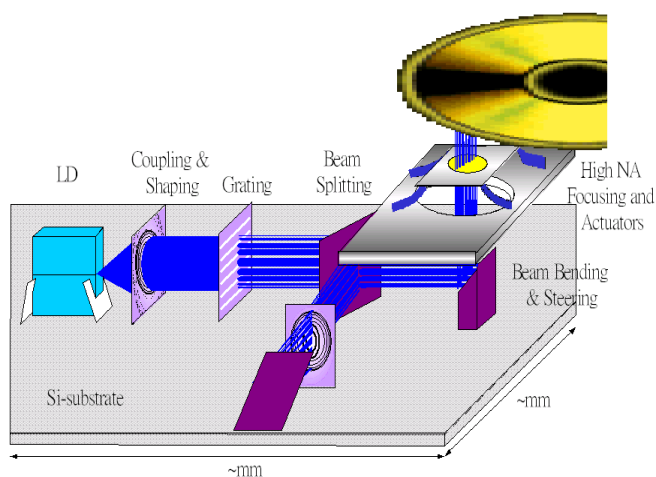
Fig. 1-3 (a) Schematic and (b) scanning electron micrograph (SEM) of a free-space optical bench [12]

Furthermore, actuators such as comb-drives, micro-motors, micromachined translational stages, and rotary stages, can be incorporated as needed into the micro-bench using the same fabrication processes. Using these available building blocks, it allows the fine adjustments in addition to coarse adjustments, which are normally achieved at the design stage using computer assisted design layout tools. Therefore, it is practical to construct a fully integrated single chip optical pickup head that includes optics, feedback electronics, and actuators.

Light from a laser diode is collimated by a Fresnel-lens, and transmitted through beam-splitter to a focusing Fresnel lens, then focused on a 45-degree inclined mirror (or a focusing Fresnel lens and 45-degree inclined mirror are combined into an inclined Fresnel reflecting lens), finally reflected upward to a rotating optical disk. The NA of the focusing micro Fresnel lens was measured to be about 0.17 [12] in this configuration.
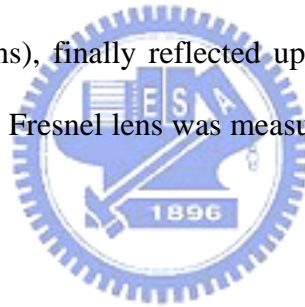
In the read mode, light is reflected from optical disk back to mirror and onto focusing micro-Frenenl lens, then transmitted back along optical axis to a beam-splitter, followed by a 45-degree mirror, finally to an integrated photodetector within substrate. The multiple segment photodetectors such as quadrant detectors are incorporated into this optical system to simultaneously detect focusing and tracking error signals, and connected with conventional detect and processing circuitry.

1.2.4 Improved free-space three-dimensional micro-pickup-head

The system shown in Fig. 1-3, adopts an edge-emitting semiconductor laser as the light source, so the intensity distribution of laser beams is elliptical and its

divergence angle is too large. To achieve more collimated and circularly-shaped beams, beam-shaping components such as a Fresnel-lens are required, but adding the Fresnel-lens will decrease the light-efficiency and increase the fabrication complexity. Besides, the heat dissipation rate of the laser diode is generally too slow because of small contact area between the semiconductor laser and substrate. Therefore, thermal accumulation decreases the lifetime of laser diode. On the other hand, the optical axis height is not controlled easily and limited by the active layer of the laser diode. To solve these issues, we proposed a novel type of micro-pickup-heads, as shown in Fig. 1.4. The module with a fiber-lens inserted in the rhombus-shaped channel is employed to solve the low heat dissipation rate of the system, and to yield incident beams with circular shape and small divergence angle. Since the laser diode is outside the pickup system, the heat from a laser diode can be dissipated efficiently. The beam focused by the fiber-lens has more circular shape and less divergence angles ($1^\circ \sim 3^\circ$). Besides, the micrograting is made of Si_3N_4, which has high transmission efficiency in the blue-laser spectrum, so the light-efficiency is high. Therefore, it can be demonstrated that our proposed system has higher efficiency and optical quality.
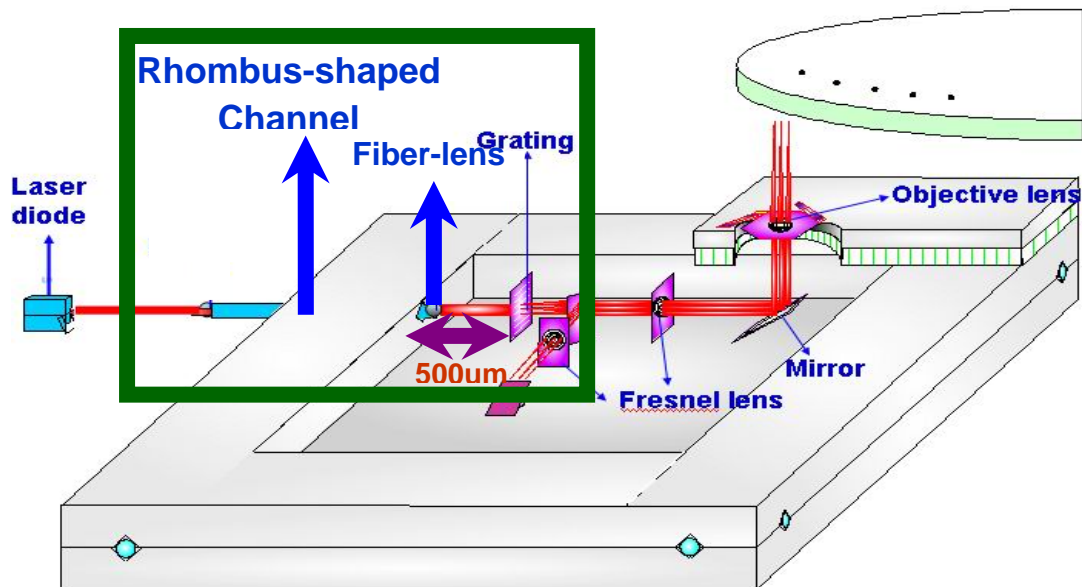
Fig. 1-4 Schematic of our proposed micro-pickup-head

1.3 Motivation and objectives of this thesis

Our proposed micro-pickup-head is also the free-space type. We used the fiberlens to guide the blue-laser beam into this free-space micro-pickup-head system. My thesis focused on the realization of these components, including the fiber-alignment structure of rhombus-shaped channels, and free-space microgratings. Optical measurement of the fiberlens and free-space microgratings is used to examine our fabricated samples, and further explore the deviation. With the demonstration of the realization of free-space components, our proposed free-space micro-pickup-head will be achieved in the near future.

1.4 Organization of this thesis

This thesis includes the following chapters. Chapter 1 introduces the current development of optical micro-pickup-heads and the objectives of this thesis. The fundamental optics of the design principles of this module will be described in Chapter 2. The simulation of microgratings will be presented in Chapter 3. The fabrication of the rhombus-shaped channel and free-space microgratings will be shown in Chapter 4. The measurement of the fiberlens and microgratings will be described in Chapter 5. Finally, a conclusion is presented in Chapter 6.

Chapter 2

Principle

2.1 Introduction

Some components of our proposed micro-pickup-head are presented in this thesis, including an edge-emitting laser source, a fiber-alignment structure, a fiberlens, and a free-space micrograting. We will explain the design principles of these components in this chapter. First, the origin and principles of collimation are presented for estimating the beam-shaping of the fiberlens. Then, gratings suitable for the optical pickup-head are discussed. Finally, it is the conclusion.

2.2 Lateral laser beam-shaping
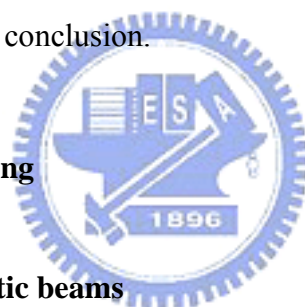
2.2.1 Collimation of astigmatic beams

The task of the beam-shaping components is to transform a non-symmetrical astigmatic laser beam into a uniform Gaussian beam. This is typically necessary for the collimation of edge-emitting laser diodes. Due to their compact and cheap manufacturability, edge-emitting laser diodes are important optical sources for a large variety of applications. However, the astigmatic characteristics of the emitted radiation will require additional optics for specific applications. Therefore, significant effort is devoted to the transformation of astigmatic and asymmetrical beam into a symmetrical and collimated beam.

The origin of the beam characteristics can be detected in the structure of the

edge-emitting laser diodes. An edge-emitting laser diode consists of a layered stack of semiconductor materials with different doping (p-n junctions). The resonator structure is oriented parallel to the layers and generally has a highly asymmetrical shape. The layer thickness representing the height of the resonator is fractions of one micron, while its width is several microns. This asymmetry of the laser resonator is the reason for an asymmetrical beam shape which upon propagation generates astigmatism due to different divergence angles caused by diffraction.

In the most general case, the shaping of such a beam into asymmetrical and collimated beam requires both amplitude and phase shaping. In order to generate the symmetrical amplitude distribution, anamorphic imaging systems are used to perform the necessary geometrical transformation. Additional microlenses are necessary to compensate for the different divergence angles in x and y [1].
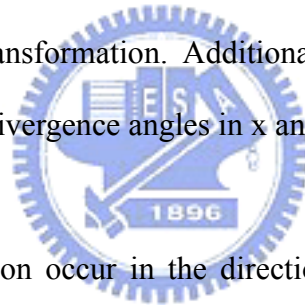
Large angles of diffraction occur in the direction of the small output window (typical values are $30° < \alpha_\perp < 60°$). The divergence in the perpendicular direction is much smaller due to the larger output window (typically $\alpha_\parallel = 10°$). Consequently, at a specific distance z_0, the beam has a symmetrical intensity distribution. Efficient shaping of the laser beam is possible with a single micro-optical element aligned at z_0 to compensate for the different phase distributions [2].

2.2.2 Design principles of the beam-shaping and collimation

In the following, we briefly outline the design process for the beam-shaping and collimated components. For the design, it is sufficient to assume a constant phase distribution at the output window of the diode. The beam profile in each dimension

13

can be approximated by a Gaussian function with widths $\sigma_{x,0}$ and $\sigma_{y,0}$, respectively. Since we assume constant phase over the output window of the laser diode, $\sigma_{x,0}$ and $\sigma_{y,0}$ are real quantities:

$$u(x,y) = A_0 e^{-\left(\frac{x^2}{2\sigma_{x,0}^2} + \frac{y^2}{2\sigma_{y,0}^2}\right)} \qquad \text{Eq. 2-1}$$

The propagation of the beam (wavelength λ) along the z-axis can be calculated by a Fresnel transform. However, since the phase distribution is no longer constant over the beam diameter the Gaussian widths are now complex quantities. For the real part of the beam width σ_x (z) and σ_y at a distance z from the diode, they are:

$$\text{Re}\left[\frac{1}{\sigma_x^2(z)}\right] = \frac{4\pi^2\sigma_{x,0}^2}{4\pi^2\sigma_{x,0}^4 + \lambda^2 z^2}; \qquad \text{Re}\left[\frac{1}{\sigma_y^2(z)}\right] = \frac{4\pi^2\sigma_{y,0}^2}{4\pi^2\sigma_{y,0}^4 + \lambda^2 z^2} \qquad \text{Eq. 2-2}$$

The plane z_0 where we wish to position the micro-optical elements is chosen in such a way that the real parts of the Gaussian widths are σ_x (z_0) = σ_y (z_0). We obtain for z_0:

$$z_0 = \frac{2\pi}{\lambda}\sigma_{x,0}\sigma_{y,0} \qquad \text{Eq. 2-3}$$

The phase profile of the beam is represented by the imaginary part of the Gaussian widths resulted from the Fresnel transform:

$$\phi_{\text{beam}}(x,z) = \frac{8\pi^3\sigma_{x,0}^4}{4\pi^2\sigma_{x,0}^4\lambda^4 z^4} + \frac{\pi x^2}{\lambda z} = \pi x^2 \frac{\lambda z}{4\pi^2\sigma_{x,0}^4 + \lambda^2 z^2} \qquad \text{Eq. 2-4}$$

Φ_{beam} (y, z) is found analogously. The beam-shaping component at z_0 is designed to compensate for the phase profile of the beam at this location (Φ_{beam} (x, z_0)). Collimation of the astigmatic beam is possible with an astigmatic microlens. Such a lens is described by two different focal lengths f_x, f_y in the two axial directions. The phase terms introduced by the lens are written as:

$$\phi_{\text{lens}}(x) = -\frac{\pi x^2}{\lambda f_x}; \qquad \phi_{\text{lens}}(y) = -\frac{\pi y^2}{\lambda f_y} \qquad \text{Eq. 2-5}$$

The two tasks of the astigmatic microlens are to compensate for the difference in the beam divergence, and to collimate the beam. It can be easily verified that a constant phase results for an astigmatic lens with the focal lengths:

$$f_x = z_0 + \frac{4\pi^2 \sigma_{x,0}^4}{\lambda^2 z_0}; \qquad f_y = z_0 + \frac{4\pi^2 \sigma_{y,0}^4}{\lambda^2 z_0} \qquad \text{Eq. 2-6}$$

The microlens described by Eq. 2-6 generates a flat phase profile over the beam diameter in the plane z_0. The phase distribution over the beam diameter is rather not important in the optical pickup heads. Therefore, single optical element performing geometrical transformations are sufficient to perform the beam-shaping. From the point of view of design flexibilities, the fiberlens is the most desirable.
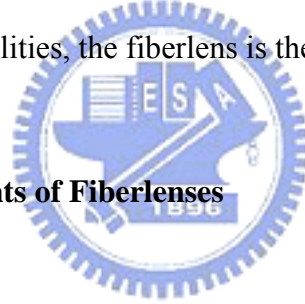
2.3 Beam-shaping components of Fiberlenses

Optical fibers have the advantages of low weight and high flexibility while used as light-guiding media, and they are inexpensive. Fibers can overcome the tight tolerance found in high numerical aperture (NA) optical path. Thus, fiber systems are good candidates for high access rate, and to be applied in the next-generation of free-space pickup-head systems.

Microlenses formed on the end of single-mode fibers (SMFs) are widely used as optoelectronic passive elements to facilitate laser-to-fiber coupling in optical communication systems. The objective of the coupling scheme is to (1) maximize the coupling efficiency, and (2) to minimize the optical feedback due to Fresnel reflection from fiber to laser. Several authors have proposed several techniques [3-8] for

producing such end-of-fiber lenses as laser-to-fiber coupling elements shown in Fig. 2-1. These techniques include photolithography [5], chemical etching [6], mechanical polishing [7], and thermal melting [8]. The radius of curvature of these lenses is only a few micrometers. These microlenses are not adequate for use in optical pickup-head systems, because they require relatively complex fabrication processes to ensure small microlens radius of curvature.
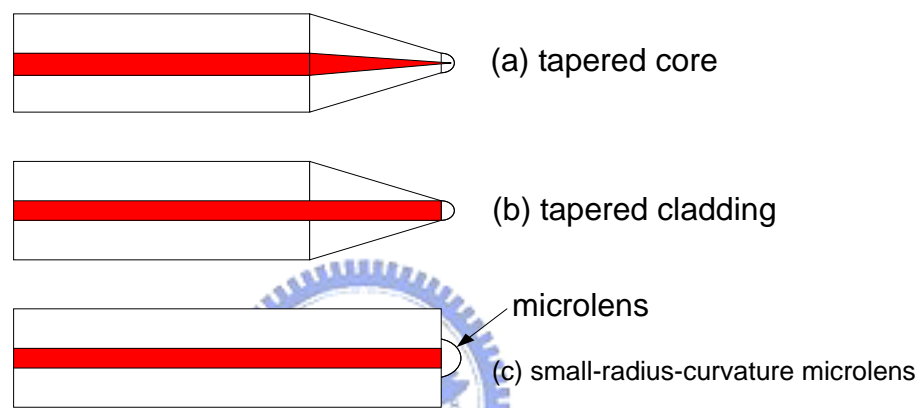
Fig. 2-1 Various conventional small-radius-curvature microlenses on the end of SMF. (a) tapered core, (b) tapered cladding, and (c) small-radius-curvature microlens

A novel design and fabrication of a microlens on the front end of a single-mode fiber (SMF) was described [9]. Its beam quality and spot size are analyzed in this section.

In our pickup-head system, a SMF with a fiber-front-end microlens is used to guide laser beams from an outside laser diode into the pickup-head, and circularizing the shape of incident beams. The objective of our scheme is to achieve the smallest spot on the three-beamed micro-grating at a reasonable working distance. The distance between the front-end of fiberlens and micro-grating is adjusted until the beam waist of focused spot is just located on the three-beamed micro-grating, because

the beam has a perfect plane wavefront at its beam waist position, while the wavefront of laser beams quickly becomes curved on both sides of the waist.

The distance between the SMF and the microlens is filled with the pure silica rod of the same diameter and same refractive index as the core of the SMF to avoid reflection, as shown in Fig. 2-2. The radius W_0 of mode field is computed by Eq. 2-7 [10]

$$\frac{W_0}{a} = 0.65 + \frac{1.619}{V^{3/2}} + \frac{2.879}{V^6}$$

Eq. 2-7

Where a=4um is the core radius of the step-index fiber, and V is the normalized frequency $V = \frac{2\pi}{\lambda} a \sqrt{n_1^2 - n_2^2}$ (n_1 and n_2 are the refractive indices of the core and cladding respectively). The mode field diameter $2W_0$ at wavelength $\lambda = 0.4$ μm is about 3.6 μm.
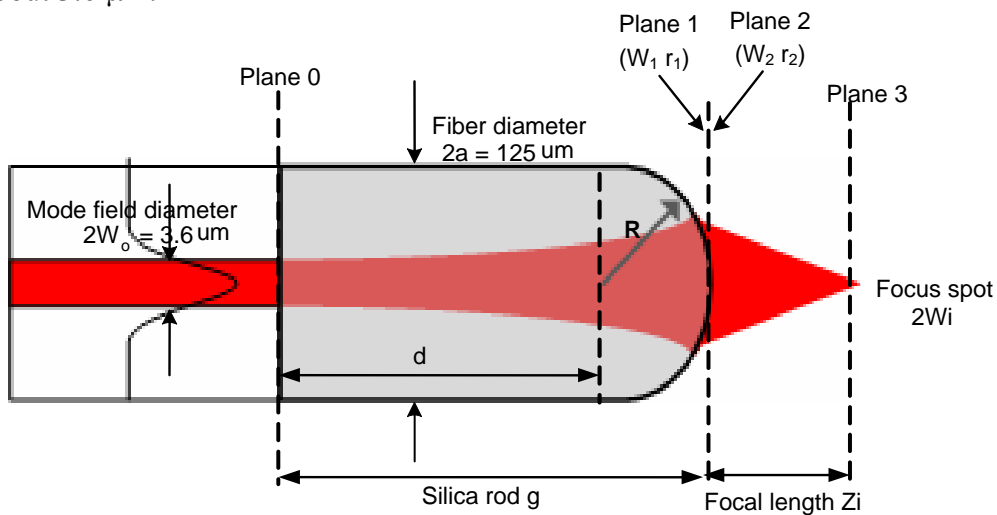
Fig. 2-2 Illustrated schematics of the microlens on the end face of the SMF (refractive index of the silica rod n = 1.47, cladding diameter 2a = 125 μm, mode field diameter $2W_0 = 3.6$ μm at $\lambda = 0.4$ μm) [9].

W_1 and r_1, beam waist and radius at output plane RP_{OUT} (Plane 1), can be expressed as

$$W_1 = W_0 \sqrt{1 + \left(\frac{g}{Z_R}\right)^2}$$ Eq. 2-8

and

$$r_1 = g + \frac{Z_R^2}{g}$$ Eq. 2-9

Where W_0 is the mode field radius of an SMF, g is the propagation distance from RP_{IN} (Plane 0) to RP_{OUT}(Plane 1), and Z_R is the Rayleigh range, where the beam diameter has the value $\sqrt{2}W_0$.

$$Z_R = \frac{\pi W_0^2 n}{\lambda}$$ Eq. 2-10

After passing through the end face of the silica rod, the radius of the beam size W_2 and the curvature r_2 at Plane 2 becomes

$$W_2 = W_1$$ Eq. 2-11

and

$$r_2 = \frac{r_1 f}{f - r_1}$$ Eq. 2-12

Where f is the focal length under paraxial approximation given by

$$f = \frac{R}{1 - n} \, (R < 0, f > 0)$$ Eq. 2-13

Where R is the radius of the plano convex lens on the fiber front end. Thus, the focused beam waist W_i and working distance Z_i can be written as

$$W_i = \frac{W_2}{\sqrt{1 + \left[\dfrac{\pi W_2^2}{\lambda r_2}\right]^2}} \qquad\qquad \text{Eq. 2-14}$$

and
$$Z_i = \frac{-r_2}{\sqrt{1 + \left[\dfrac{\lambda r_2}{\pi W_2^2}\right]^2}} \qquad\qquad \text{Eq. 2-15}$$

respectively.

A hemispherical microlens at the front end is used as the focusing element. The length of the pure silica rod d is designed to control the focused beam waist W_i, which is defined as half-width at $1/e^2$ maximum intensity, and position Z_i, which is defined as the distance from the beam waist position to the front end of the lens. The relationship of W_i and Z_i is a function of propagation distance $g = d + \mathbf{R}$, where $\mathbf{R}$ is the radius of the hemispherical lens.
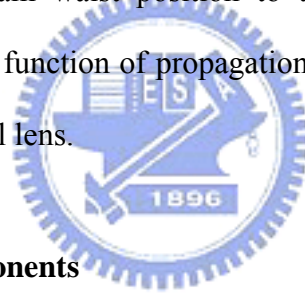
2.4 Diffractive optical components

The beam-splitters must provide good extinction ratio, a broad wavelength range for operation with broadband source, a large angular tolerance and a small size for effective packaging. Conventional beam-splitters are based on the use of the natural birefringence of crystals (Wollaston prisms, for example) or in the use of the polarization selectivity of multilayer dielectric coatings. Diffractive optical elements (DOEs) are attractive because they can solve problems of compactness inherent to the use of MOEMS processes and are adapted to mass production. In some implementations of DOEs, the two orthogonally polarized optical fields of TM and TE are both reflected, while in some cases both are transmitted, and in yet another category, one is reflected and the other transmitted.

The potential of diffractive optics lies in the fact that any phase profile can be fabricated as a DOE, even if refractive implementation is impossible due to constraints in the fabrication process. Most of the microlithographic techniques for pattern transfer are optimized for the fabrication of grating step profiles. The fabrication is possible with the same technological approaches of phase quantization, independent of the functionality. On the other hand, DOEs for any functionality can be implemented optimally, and reduce the number of optical elements required because they perform complex phase transformation that are not possible with refractive optical elements (ROEs). Besides, the DOEs have less aberration than the ROEs. In Fig. 2-3, we summarize some of the frequently used types of DOEs,

(a) The 1*3 beam-splitting gratings, which are general gratings with constant periods, can be used to replace the conventional beam-splitters. Their periods and diffraction angles can be evaluated according to the grating formula: $2d\sin\theta=m\lambda$

(b) The 1*N beam-splitter gratings with variant periods perform multiple beam -splitting.
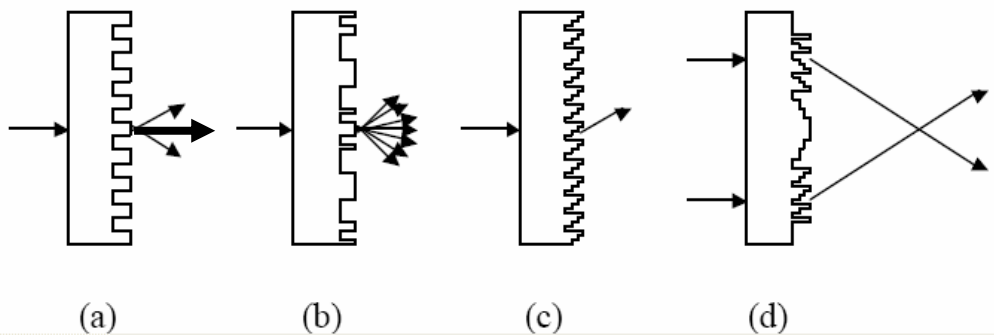
Fig. 2-3 Examples of DOEs: (a) 1*3 beam-splitter; (b) 1*N beam-splitter (e.g., Dammann grating), (c) beam deflector, and (d) diffractive lens (e.g., Fresnel lens).

(c) The beam deflectors with multiple steps within a period are used to approximate the reflected blazed gratings.

(d) The diffractive lens such as a Fresnel lens performs focusing.

2.4.1 Transmission gratings

As with any grating, the objective of transmission gratings is to control the division of incident light into the various orders beams. Diffraction efficiency describes the fraction of the incident light that is diffracted into the orders of use at the wavelength band. The efficiency of transmission gratings mainly depends on groove geometry, with the physics of transmission gratings simpler than for reflection gratings because there is no metal surface. Therefore, they operate largely in the scalar domain due to the near absence of polarization effects.

Phase gratings only change the phase of the incident light in the different groove regions, and amplitude gratings are presumed to change the amplitude. It means that phase gratings have variation of the real part of the refractive index of the grating material, while amplitude gratings vary in the imaginary part. The incident beams diffracted through amplitude gratings will be absorbed or reflected partially, so that its light-efficiency is lower than phase grating. Besides, phase gratings are generally adopted because their optical behavior is controlled by the physical phase retardation. Amplitude gratings, or Ronchi rulings, have a line pattern that is alternately opaque and transmitting and therefore low diffraction efficiency. Their maximum first order efficiency is about 11%, and naturally occurs when the filling factor is 50%. Under this condition, the sum of the zeroth and two first orders is about 47.6%, which implies that the sum of all remaining orders is only 2.4%, because even orders vanish

under ideal conditions and odd orders decrease rapidly with the square of diffraction order values.

Transmission gratings are usually classified as rectangular, sinusoidal, triangular and other groove shapes. At normal incidence the symmetry of rectangular or lamellar gratings leads to equal energy in both plus and minus first orders, while the fraction devoted to the zero order at one wavelength can vary from near 0 to over 90%. Sinusoidal gratings share the property of symmetry, but not quite the wide control over zero order. Cylindrical sections or parabolic grooves with several segments of different angles are called multiple order transmission gratings or fan-out gratings, and they are generally designed to split 5 to even 20 orders beams with their intensities as equal as possible.
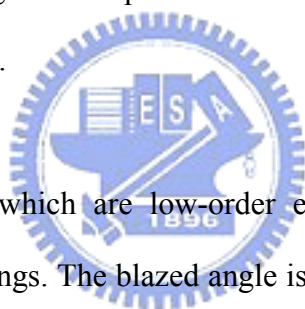
The echelette gratings, which are low-order echelle gratings, have the well known profile for blazed gratings. The blazed angle is defined as the diffraction angle of the wavelength whose efficiency is maximal. Blazed or triangular gratings can serve as efficient and compact beam-dividers for monochromatic light, especially when the angle between the beams is to be small and well-controlled. They are also designed to deliver a particular ratio of first to zero order at a constant wavelength. Bragg-condition gratings usually deliver exceptionally high first order efficiency in both planes of polarization, and high diffraction angles. Zero order diffraction (ZOD) gratings are used to vary intensity of zeroth order from zero to unity at a specific wavelength, and therefore enable construction of high contrast optical transmission filters such as subtractive color filters. With incident white light illuminating in subtractive color systems, cyan (minus red), magenta (minus green), and yellow (minus blue) can be obtained from the three primary colors.

In summary, symmetric transmission gratings are used as beam splitters for optical pickup heads, where the wavelength of the laser source is constant, since the efficiency of plus and minus first orders must be equal as possible.

2.4.2 Grating anomalies

An ideal grating is one of infinite size with perfectly uniform groove spacing, and uniformly illuminated with collimated light. It is designed to diffract only in the directions dictated by the grating equation. However, in practice the finite size of real gratings will generate small secondary maxima between the diffraction orders. Therefore, the back face of a grating needs an anti-reflection coating, usually with a resin transparent at the operating wavelengths, to prevent light loss due to reflection, and to avoid multiple scattering effect inside the grating.

Grating anomalies significantly degrade the optical behavior of gratings, as is the case with surface wave and non-linear second-harmonic generation. Besides, spectral purity or the absence of stray light describes the signal to noise, and is strongly related to the uniformity of groove spacing. Moreover, the corrugation and holes in the grating surface, inherent to the fabrication error or probing the grating, should be eliminated with the CMP (Chemical Mechanical Polishing). But the CMP machines are available only to 6 inches wafers in NDL. Therefore, our microgratings necessarily have serious aberration inherent to the fabrication errors.

2.5 Summary

As discussed above, the design principles of beam-shaping components of fiberlenses are mentioned. The recognition related to gratings is necessary for designing and fabricating gratings suitable for the pickup-head. We adopted symmetric transmission microgratings as the beam-splitter in our proposed optical pickup-head.

The grating designed in this thesis is according to *Rigorous Coupled Wave Analysis* (RCWA), which is a more accurate solution of Maxwell's equations [11] [12]. Since the package software, GAOLVER, based on RCWA is already available to the analyses of diffraction, there is no further introduction about RCWA in this thesis. We used the software, GAOLVER, to perform the simulation which will be discussed in detail in chapter 3.
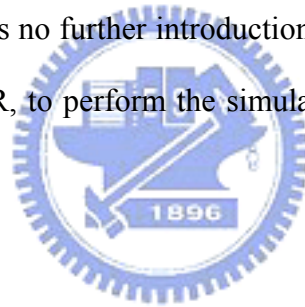
Chapter 3

Simulated Results

3.1 Introduction

In the pickup-head system, the gratings have been widely used as beam-splitters to divide into three beams for tracking error detection. We will discuss the design of microgratings in this chapter. First, the simulation tool, GSOLVER software, will be briefly introduced. Then, we use GSOLVER to calculate the optical performance of our micrograting. The parameters considered in our design, includes the material, period, thickness, and filling factor of the micrograting. Finally, a brief summary about the micrograting will be given.
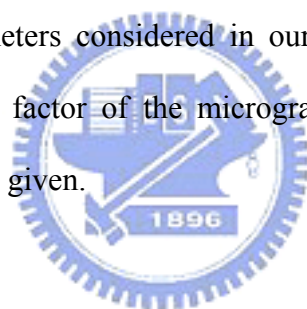
3.2 Simulation Tool

GSOLVER software is an analytic tool available to diffraction simulation of gratings. It calculates diffracted fields, phases, and diffraction efficiency of plane wave illuminated to arbitrarily complex grating structures, while the illumination may be at any incidence (conical mounts) and any polarization (TE, TM, circular, or elliptical). The grating structure is defined by a piecewise constant approximation, so that it permits the analyses of simple classical grating profiles (blaze, sinusoid, holographic, binary, 3-point plotline, etc), and complicated structures (multi-layers, coatings, interweaving of material, shadows, etc).

GSOLVER employs full 3D rigorous coupled wave algorithm (RCWA), which can be applied to explaining the diffraction phenomenon of gratings. We will not discuss further theory of RCWA here, since the derivations of these equations are too complicated to be introduced here. The references of RCWA theory will be listed in the Appendix 2. Thus, for the pickup head, by calculating the energy distribution of all retained diffraction orders beams, the features of microgratings will be optimized in the following sections.

3.3 Material and dimension of microgratings

To achieve simultaneously high light-efficiency, expected energy distribution and realization of fabrication, the structure of microgratings, including their period, filling factor, and thickness, must be optimized. Thus, these parameters and material of microgratings will be determined in the following sections.
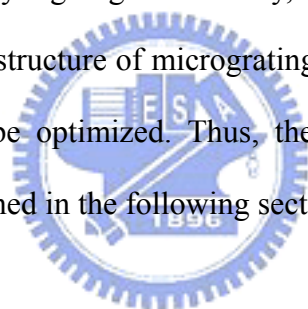
3.3.1 Material of microgratings

While most transmission gratings are used in the visible light spectrum, it is possible to extend their performance into the near UV (250nm) and near IR (2.5um), with choices of appropriate materials. Generally, maximum value of diffraction efficiency depends somewhat on the refractive index of the grating, in that lower index leads to greater efficiency, due to reduced backward diffraction that results from lowered reflectivity. But decreasing the index also calls for increased grating depth, while thick layers tend to have rough surface and even cracks or corrugation.

In the surface-micromachining processes, generally, SiO_2 layers are applied to

the sacrificial layers, and Si_3N_4 layers are used as the structures or electric insulation. Contrast to the poly-silicon, Si_3N_4 has higher transmission efficiency in the blue-laser spectrum. Compared with the photoresist, the thickness of Si_3N_4 layers can be controlled more accurately by LPCVD than the photoresist by the spinner, since the thickness of microgratings mainly determines the optical property. Although isotropic O_2 plasma is used to trim the profiles and thickness of the grating ridges, unstable etching will reduce both the width and the height of the remaining photoresist ridges, and hence affect the filling factor of the final grating. Besides, due to the natural photoresist behavior, the groove form can not be easily manipulated, so that results differ from sample to sample. Compared with main kinds of materials applied to MOEMS process, as shown in Table 3-1, the nitride has high transmission light-efficiency in the blue-laser spectrum and is well-suitable for the surface-micromachining processes. Therefore, Si_3N_4 is a preferred candidate as the material of our micro-grating.
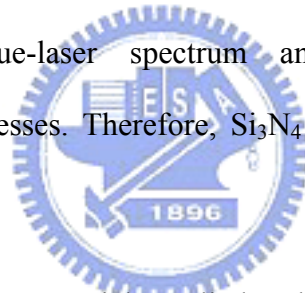
Table 3-1. Contrast between the materials applied to the surface-micromachining process [1].

Material	SiO$_2$(glass)	poly-silicon	photo-resist	Si$_3$N$_4$
Transparent region (um)	0.16~8	1.1~14	broad	0.25~9
Control of layer thickness	PECVD	LPCVD	Spinner	LPCVD& H$_3$PO$_4$ etching
Role in surface micromachining process	Sacrificial layers	Structure	Structure	Structure & electric insulation

The Si$_3$N$_4$ layers are deposited in NFC (Nano Facility Center). Generally, the Si$_3$N$_4$ layers applied to structures are deposited by LPCVD, since ones achieved by PECVD (Plasma Enhanced Chemical Vapor Deposition) have considerable tensile or compressive stress. Generally, it is compressive stress when the deposition temperature is of less 350 ℃, while tensile stress exists at high deposition temperature, as shown in Fig. 3-1. The Si$_3$N$_4$ layers by LPCVD are belong to the Si-rich-Si$_3$N$_4$, and they have higher refractive index (n=1.96~2.2) and lower residual stress than N-rich-Si$_3$N$_4$, while large residual stress will result in degrading optical property of components. Besides, the thickness of Si$_3$N$_4$ layers can be trimmed by the wet-etching of 86% H$_3$PO$_4$ (the etching rate is 8.1nm/min at 180℃) or BOE (the etching rate is 57nm/min at 25℃). Therefore, the material of our micrograting is low-stress Si-rich-Si$_3$N$_4$ deposited by LPCVD.
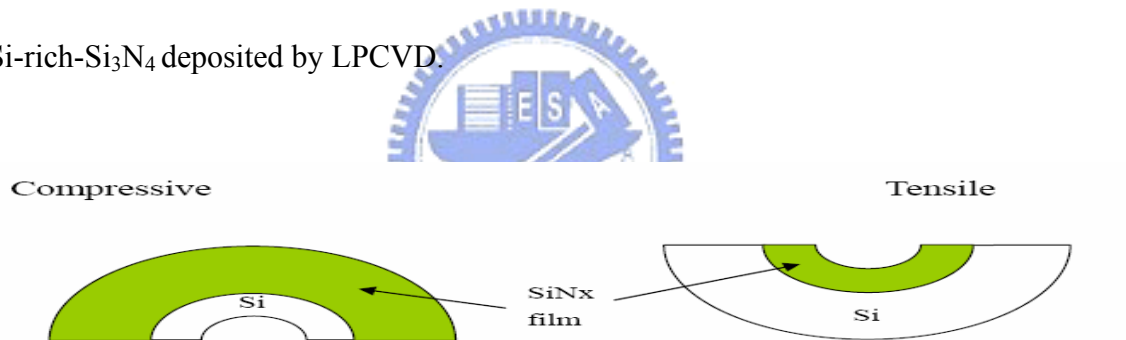
Fig. 3-1 Compressive stress and tensile stress

3.3.2 Period of microgratings

For the tracking error detection, the grating is one of key components used to divide into three beams in the pickup-head system. As a rule, the zeroth order beams read the data pitches of compact disk, and the two first order beams read adjacent pitches to keep the head both centered and focused, as shown in Fig.3-2. Therefore, since diffraction efficiency of +1 and -1 orders must be equal, the profile of transmission gratings is symmetric, necessarily.

In the next-generation optical storage system, the distance between adjacent pitches is 5um, and the focal length of objective lens must be 100*n um at least, where n is the refractive index of the substrate. For the next-generation optical storage disks (Philips and Sony proposed), diffraction angle of gratings between the zeroth order and +1 or -1 order beams is $5*10^{-2}$ radians or $2.86°$ (commercial specifications) at least, as shown in Fig. 3-3. The following formula is the grating equation:

$$n_1\sin\theta_1 = n_2\sin\theta_2 + m\lambda/d \text{ , } \qquad m=0, 1, 2.....,-1,-2........, \qquad \text{Eq. 3-1}$$

where n_1 the n_2 are the refractive indices of grating and ambience, θ_1 and θ_2 are the angles between the incident (and the diffracted) wave directions and the normal to the grating surface, λ is the wavelength, d is the grating period measured in um, and m is the order of diffraction.

According to Equation 3-1, the period of rectangular gratings is about 8 um. We set the diffraction angle between the zeroth order and the ± 1 orders beams to be $2.9° \pm 0.1°$. Thus, the period is 8um $\pm$ 0.25um, where the grating period in our mask is 8um and the fabrication tolerance is 0.25um.

3.3.3 Thickness and filling factor of microgratings

Since the thickness and filling factor of gratings mainly determine the diffraction efficiency, and they are affected greatly by the quality of fabrication, they are chosen as the main variables of GSOLVER simulation. The relationship between the thickness and diffraction efficiency was simulated at different filling factor ranging from 0.3 to 0.7, respectively. For evaluating diffraction efficiency and these two

variables simultaneously, the results of GSOLVER simulation were plotted as the contour diagrams by the Sigma-Plot software according to the distribution of diffraction efficiency ratio values, as shown in Figs. 3-5, 3-6, 3-7, 3-8, 3-9, 3-10. The simulated results of diffraction efficiency distribution in the blue-laser spectrum were shown in Figs. 3-5, 3-6, 3-7, while Figs. 3-8, 3-9, 3-10, were in the red-laser spectrum. In those figures, the green region represents these ratio-values ranging from 6 to 12 for the pickup head, while the blue and red areas represent ratio-values smaller than 6 and larger than 12, respectively. We further contoured the green region by the ratio-values difference of 1 to hold elaborately the distribution of diffraction efficiency ratio.

According to the thin-grating theory, the distribution of maximal diffraction efficiency is described as the following equation:
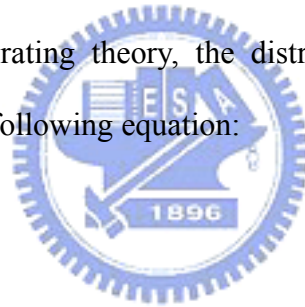
$$t = \frac{m\,\lambda}{n-1}$$ **Eq. 3-2**

, where t is the thickness of thin gratings with maximal diffraction efficiency, λ is the wavelength of incident beams, n is the refractive index of thin gratings. We adopted that the wavelength of incident beams was 405nm, and refractive index of Si_3N_4 was 2.1, so the maximal diffraction efficiency happened when the thickness of thin gratings was 0.37um, 0.75um, 1.11um, etc. But the diffraction efficiency ratio was from 6 to 12 only when the thickness of thin gratings was about 0.75um.

For improving the feasibility of expected micro-gratings, these parameters in the green region having larger area, were used to realize the micrograting. From these simulated results, the micro-grating is the most suitable for the pickup head when its thickness is 0.75um, since filling factor ranging from 0.4 to 0.6 still serves the

objective at that thickness, while larger range of filling factor represents larger process tolerance. Therefore, our micrograting was designed to have filling factor of 0.5 and grating depth of 0.75um. Besides, the micrograting is still suitable for the pickup-head in the red-laser spectrum. Therefore, this micrograting can be broadly applied to pickup-head systems, whether their light-source is blue-laser or red-laser.

Because the free-space micrograting may not stand vertically to the substrate due to the fabrication error, the incident beam does not propagate normally to the grating. Therefore, the GSOLVER simulations at different angles were required to explore the incident-angle tolerance. From the simulation, we concluded that the incident angle tolerance was as high as 15 degrees.
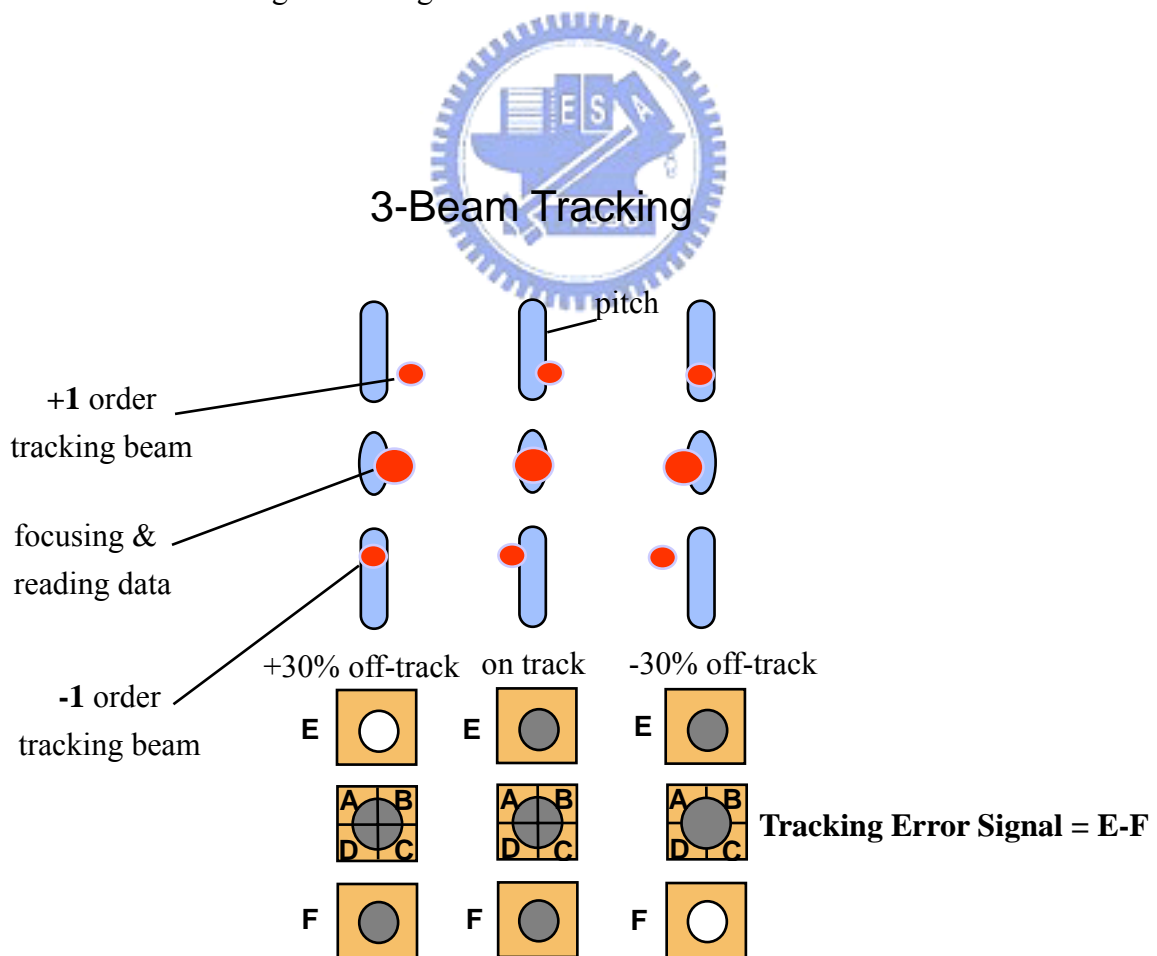
Fig. 3-2 Three beams method for the tracking error detection.

Objective lens of pickup-head

0 order beam

+1 order beam

diffraction angle
$\Theta = 2.86°$

Optical-axis

HDDVD pitch

5um

0.3um

Distance ≧ 100um
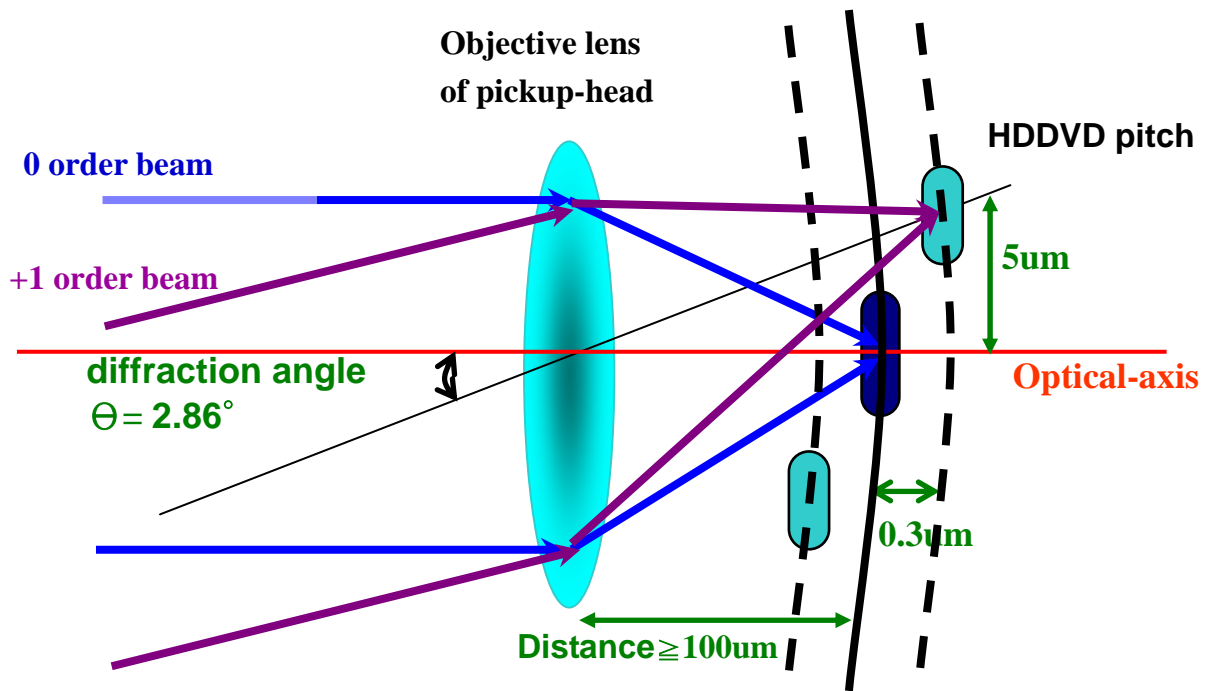
Fig. 3-3 Schematic of the optical path of the next-generation optical storage system, where θ represents the diffraction angle between the zeroth order and the ±1 orders beams.

3.3.3.1 Thickness of microgratings

The proper thickness of gratings will enhance the diffraction efficiency and split beams at the optimal ratio suitable for the pickup heads. For the pickup head, the diffraction efficiency ratio of gratings is 6~12 (commercial specifications) between the zeroth order and the ±1 orders beams, as shown in Fig. 3-4.

Light source

Grating

Diffraction efficiency ratio of $\dfrac{0\text{order}}{+1\text{order}}$

+1 order   1
0 order   6~12
-1 order   1
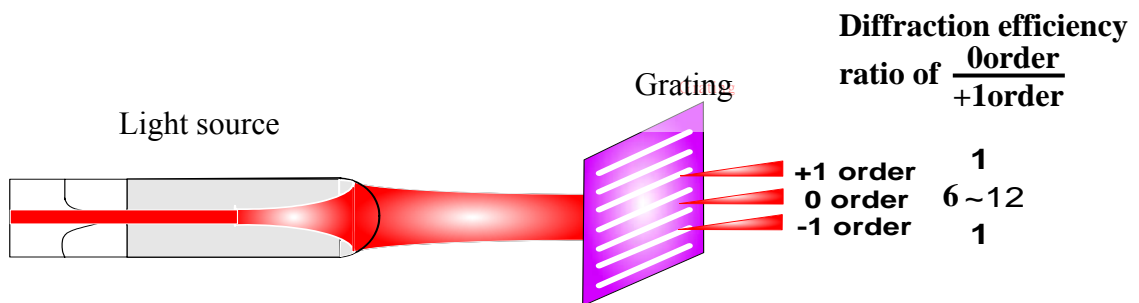
Fig. 3-4 Target of energy distribution of the three-beamed micrograting

According to the contour diagrams (Figs. 3-5, 3-6, 3-7, 3-8, 3-9, 3-10), the thickness of Si_3N_4 layers should be 0.75um $\pm$ 0.05um, where the filling factor of micrograitings is 50%. Namely, the target of film thickness can be set to be 0.75um, and the fabrication tolerance is 0.05um. The thickness of Si_3N_4 layers can be easily controlled by selecting suitable LPCVD deposition time. Once the Si_3N_4 film is thicker than 0.75um, H_3PO_4 or BOE is used to trim the thickness.

3.3.3.2 Filling factor of micrograitings

In the fabrication flow, the linewidth of components tends to vary in photolithography and RIE steps. Therefore, the tolerance of the filling factor must be detected. According to the contour diagrams (Figs. 3-5, 3-6, 3-7), when the filling factor is from 40% to 60%, the diffraction efficiency ratio still meets the objective. Namely, this range indicates that the linewidth of grating ridges can be varied from 3.2um to 4.8um without huge deviation of energy distribution, when the ridges length of micrograitings is 4um. Generally speaking, the tolerance of 0.8um is achievable.

3.4 Summary

For the pickup-head, we designed a micrograiting made of Si_3N_4 to achieve the expected diffraction efficiency ratio (6~12) between the zeroth and the $\pm$1 orders beams. According to the distribution of diffraction efficiency ratio, the thickness of 0.75um is preferred in the blue-laser or red-laser spectrum, where the period is 8um $\pm$ 0.25um, and the incident angle of blue-laser beam is of less than 15°. Considering the process tolerance in advance, the feasibility of expected energy distribution of diffracted beams can be realized.

Fig. 3-5 Distribution of diffraction efficiency ratio between the zeroth and two first orders beams. GSOLVER simulation condition：$\lambda = 405nm$，period=8um，material is Si_3N_4，diffraction angle is 2.9°，and the incidence angle is 0°.
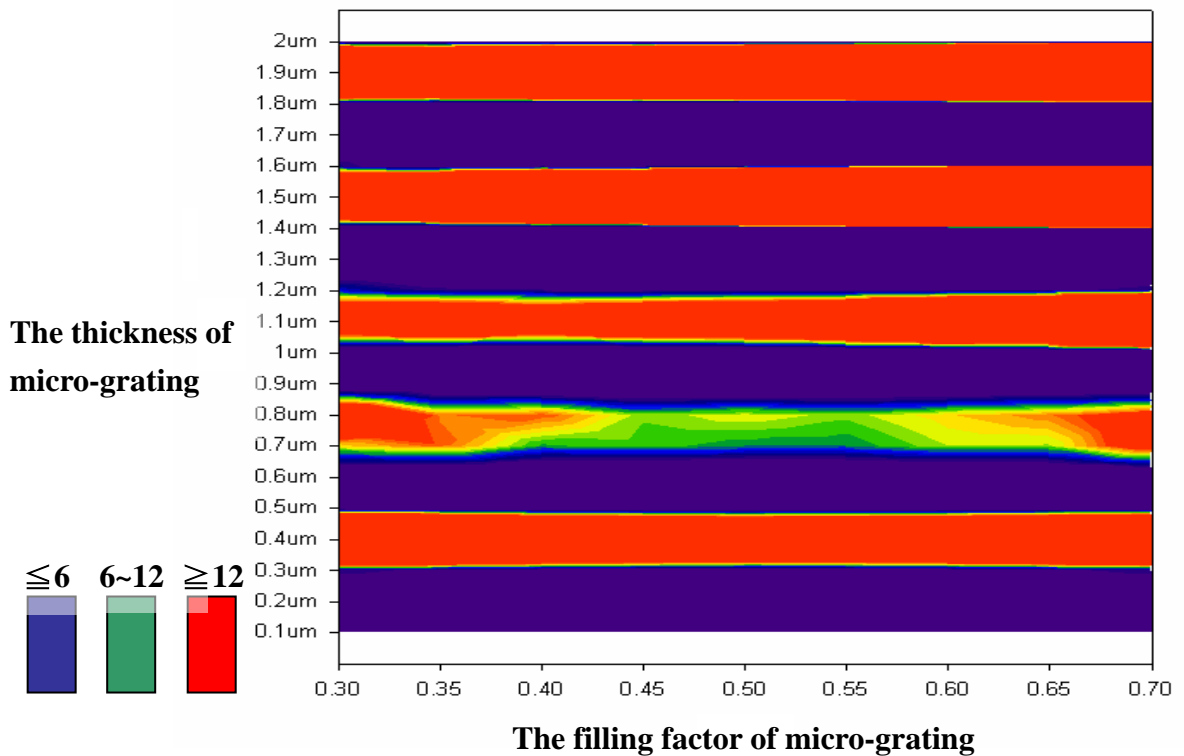
Fig. 3-6 Distribution of diffraction efficiency ratio between the zeroth and two first orders beams. GSOLVER simulation condition：$\lambda = 405nm$，period=8um，material is Si_3N_4，diffraction angle is 2.9°，and the incidence angle is 5°
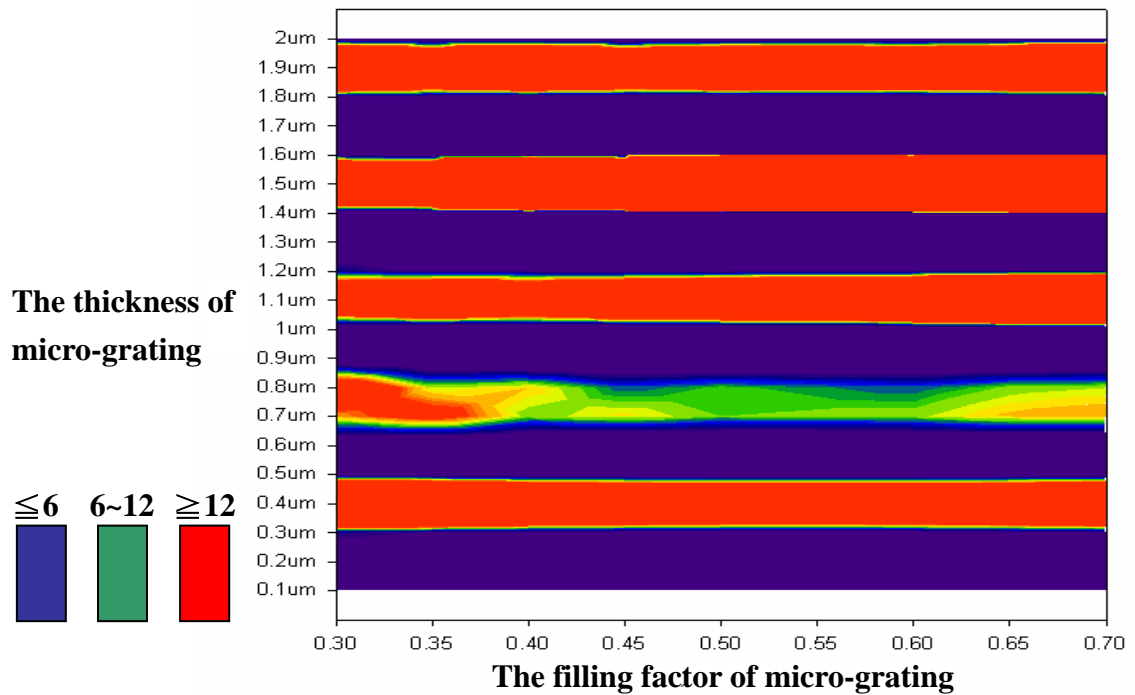
Fig. 3-7 Distribution of diffraction efficiency ratio between the zeroth and two first orders beams. GSOLVER simulation condition：$\lambda = 405nm$，period=8um，material is Si_3N_4，diffraction angle is $2.9°$，and the incidence angle is $10°$
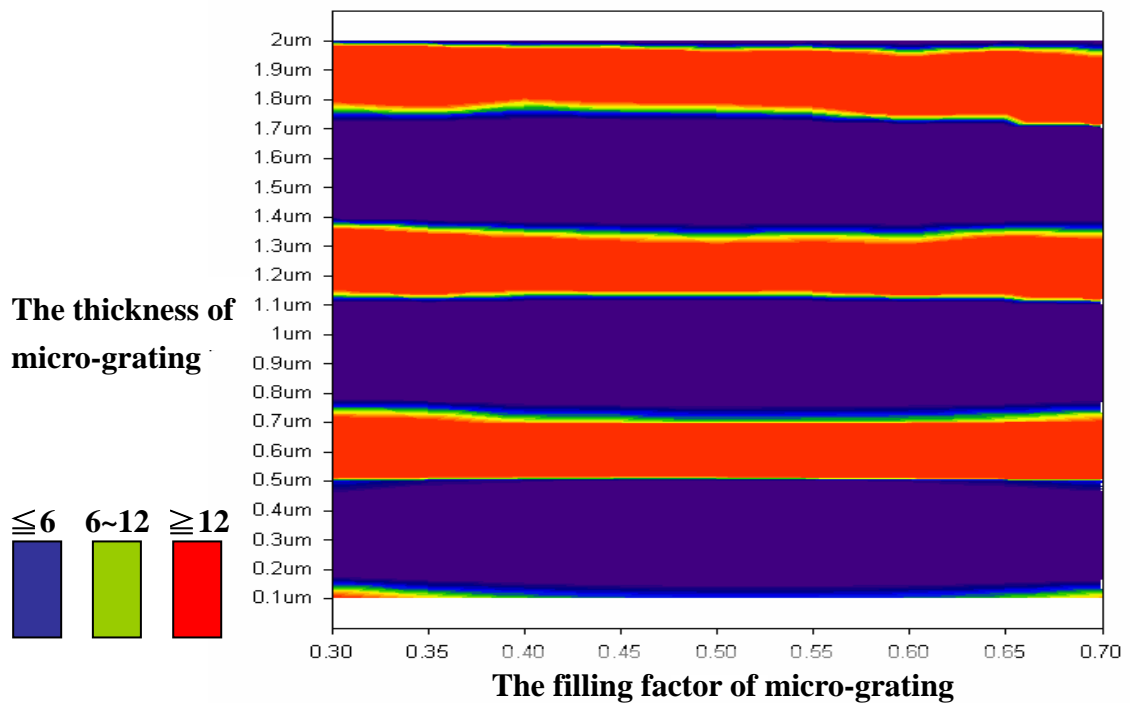
Fig. 3-8 Distribution of diffraction efficiency ratio between the zeroth and two first orders beams. GSOLVER simulation condition：$\lambda = 633nm$，period=8um，material is Si_3N_4，diffraction angle is $4°$，and the incidence angle is $0°$.
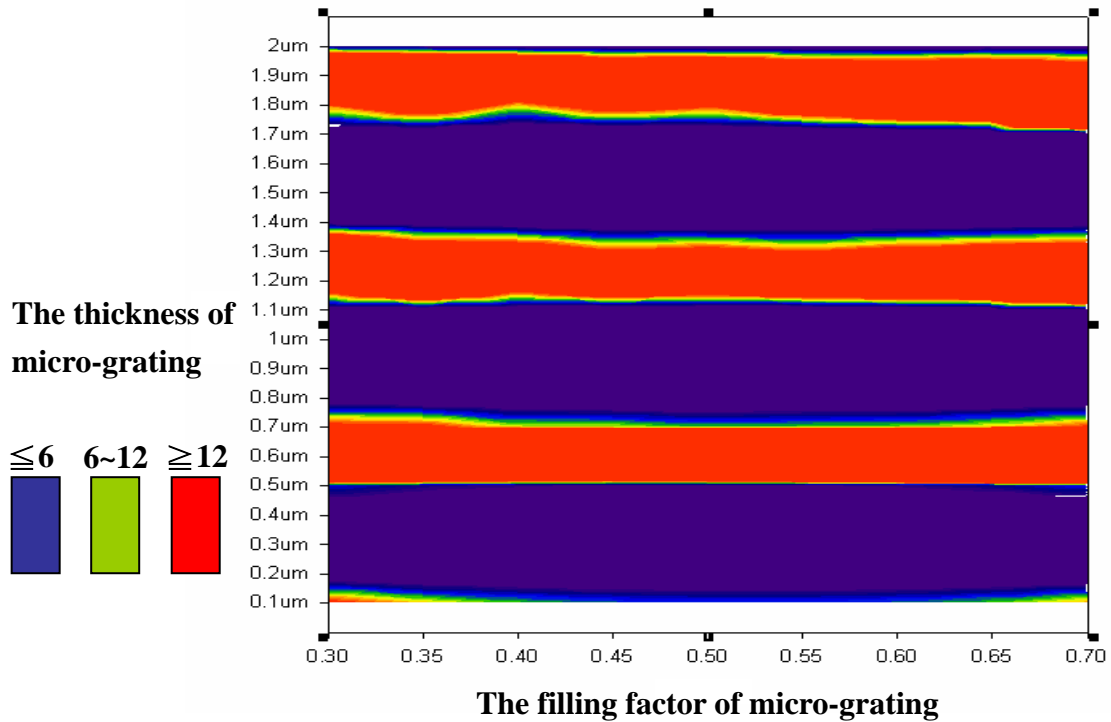
Fig. 3-9 Distribution of diffraction efficiency ratio between the zeroth and two first orders beams. GSOLVER simulation condition：$\lambda = 633nm$，period=8um，material is Si_3N_4，diffraction angle is $4°$，and the incidence angle is $5°$.
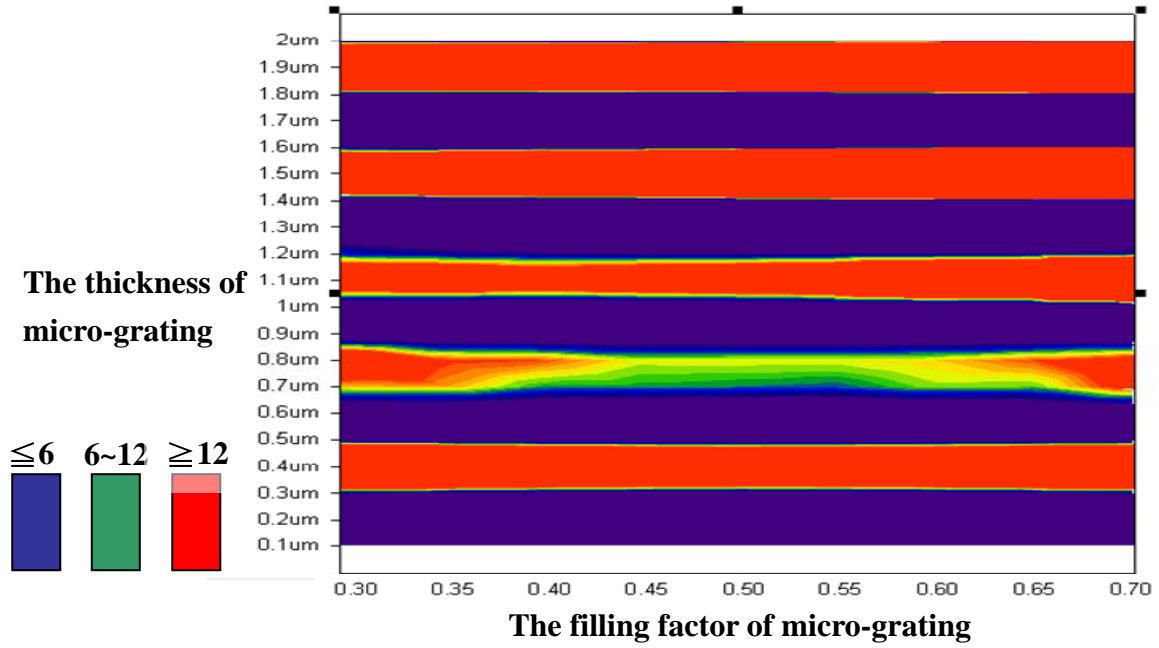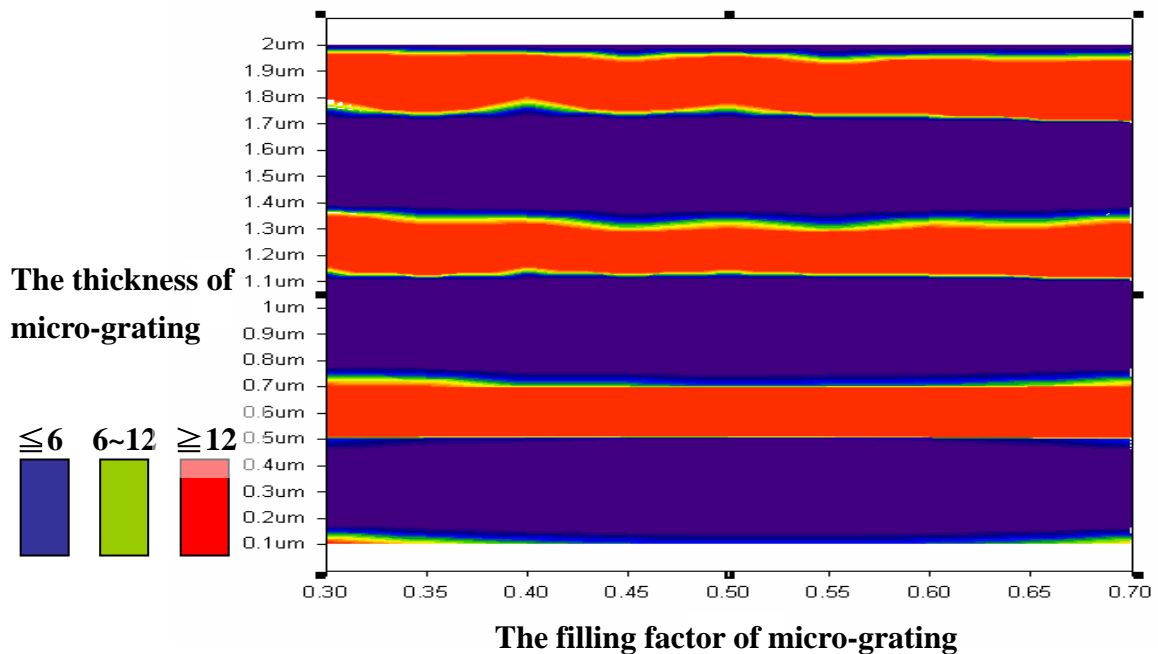

Fig. 3-10 Distribution of diffraction efficiency ratio between the zeroth and two first orders beams. GSOLVER simulation condition：$\lambda = 633nm$，period=8um，material is Si_3N_4，diffraction angle is $4°$，and the incidence angle is $10°$

Chapter 4

Micro Fabrication Processes

4.1 Introduction

The fabrication technologies for the fiber-alignment structures and free-space microgratings will be presented in this chapter. The rhombus-shaped channels were fabricated for inserting the fiberlens. The out-of-plane micrograting made of Si_3N_4 was realized by the MOEMS process and the probe system. Finally, the future work and a brief summary were described.
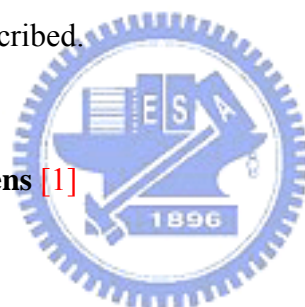
4.2 Fabrication of the fiberlens [1]

The fabrication of the hemispherical-shaped fiberlens was mentioned in detail in [1]. We will directly adopt the fiberlens without further introduction of its fabrication process.

4.3 Fabrication of the rhombus-shaped channel

Anisotropically etched V-grooves in silicon or precision-machined glass blocks are widely used for this purpose of placing the fibers. These drawbacks of V-grooves are that the vulnerable bare fibers placed on top of the wafer, and shear stress produced by the dried resins. Although alternative technologies [1][2][3] such as adding plate on top of the groove were developed to fix the fibers mechanically within

the V-grooves, their fabrication is complex and these additional mechanisms can neither hold the fibers accurately.

A fiber alignment structure, with precise rhombus-shaped channels [4] formed by {111}-equivalent planes within {100}-silicon, is proposed in our novel optical pickup head module shown in Fig.1-4. Compared with the V-groove channels, the fibers are totally buried and thereby protected. Therefore, the rhombus -shaped channels are suitable for the hybrid integration of other components on their top surface, and allow a simplified assembly of fiber ribbon arrays due to integrated funnels for fiber insertion. Besides, adding resins on the fiber in the V-groove will result in reliability problem due to shear stress. However, the upper parts of rhombus provide the support force and precise alignment to the fiber, so the position of the fiber is more precise as shown in Fig. 4-1(a). Therefore, the rhombus-shaped channels are adopted for the fiber -alignment structures in our pickup head system.
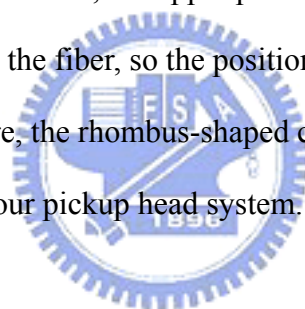
Rhombic channels were first demonstrated in silicon using laser melting [5]. Alternative, deep silicon etching as well as wafer dicing can be used for the pre-structuring step. The vertical-anisotropic pre-structuring step causes a deep crystal damage that allows the wet etching to attack deeper areas of the wafer. A rectangular damage such as a trench in {100}-silicon aligned along the (110)-flat directly defines the shape and size of the rhombus. A small but deep trench results in a nearly closed rhombic channel, while a broad but shallow trench ends up in a V-groove. The final size of the rhombus is defined by the width w of the opening at the wafer and the depth d of the trench. The minimal depth has to be

$$d = \frac{2r}{\cos(\alpha)} - w \cdot \tan(\alpha) = \sqrt{3} \cdot 2r - \sqrt{2} \cdot w \qquad \text{Eq. 4-1}$$
$$\text{for } \alpha = 54, 74° \text{ in } \{100\}\text{-silicon}$$

If the trench width is equal to the mask opening, a standard single-mode fiber is completely buried below the wafer surface for d = 2r =125um and w = 2r*tan(α /2) = 64.5um. A comparable V-groove would be as wide as 241 um, a U-groove requires 125um at least. If the trench width is smaller than the mask opening mainly due to the issues of lithography and etching, the depth has to be increased properly. The mask opening w precisely defines the two upper {111}-planes of the rhombus that provide the necessary precision for the alignment of fibers. If w varies by △w, the fiber core position is vertically shifted by △y = √2*△w, as shown in Fig 4-1(b). The achievable accuracy of rhombus -shaped channels can directly be examined by measuring the width w of the slit after KOH etching. Therefore, the axis height of optical systems can be controlled precisely.
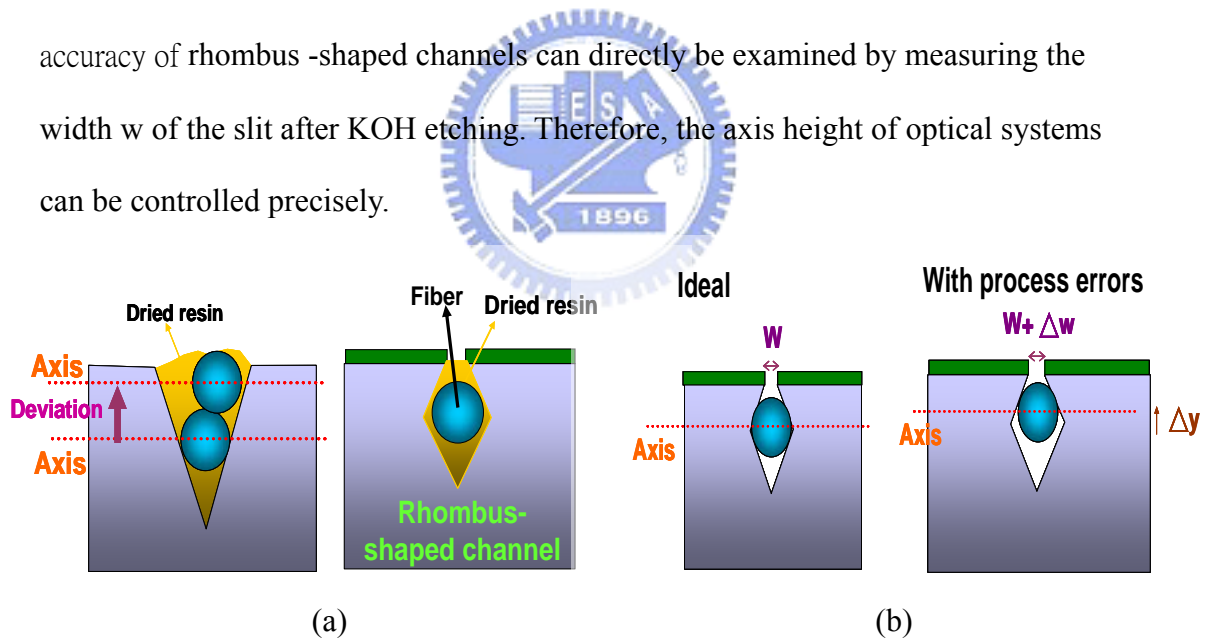
Fig. 4-1 (a) The position of the fiber in the V-groove has huge deviation due to shear stress, and (b) the accuracy of rhombus-shaped channels can directly be examined by measuring the width of the slit after KOH etching.

The rhombus-shaped channels are fabricated with the bulk-micromachining technique. The fabrication process is illustrated in Fig. 4-2. First, a 0.5um layer of

nitride (Si_3N_4) deposited by LPCVD was used to resist the anisotropic-etching of KOH. Second, the width of trenches was defined with the photolighography. We adopted a layer of thick-photoresist AZP4620 spun up to 6um onto the chip as the mask layer of the Deep-RIE and ICP. The Deep-RIE (reactive ion etching) opened the silicon nitride mask, and this step determined the overall accuracy of rhombus -shaped channels. After that, the expectant trench depth was achieved using the ICP (Inductively Coupled Plasma). Another approach to achieve the necessary trench was that milling with a wafer-dicing saw, which was more expensive but inaccurate than ICP. Finally, according the simulation of Intellisuite software, the rhombus-shaped channel was structured optimally by the anisotropic wet etching of 20% KOH solution at 60℃ in about 2 hours. The etching stops stably at {111}-planes, which are arranged under an angle of 54.7° against the surface forming a rhombus.
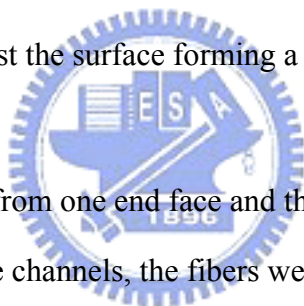
The fibers were inserted from one end face and threaded easily without dedicated tools. Once introduced into the channels, the fibers were hold in the rhombus-shaped channels. After adding glue or resins, the fibers were slightly pressed into the upper part of rhombus due to the shear stress from the dried glue or resins. The excess glue or resins can escape through the slit of the top surface. A variety of glues can be used to fix the fibers in the rhombus, especially epoxy resins and UV-curing glues. We adopted epoxy resins called Acryfix that are hardened in 15 minutes at 25℃.

After fiber assembly, the quality of the mounting process is proven by cutting the glued channels. No residual film between the fiber and the upper part of rhombus is found and the cavity is completely filled with hardened resins. The deviation of the core position of the fibers results from misalignments during the fabrication flow, the fiber gluing process and inaccuracies of the fibers (diameter and core position).

(a) Step 1. 0.5um nitride layer deposited by LPCVD
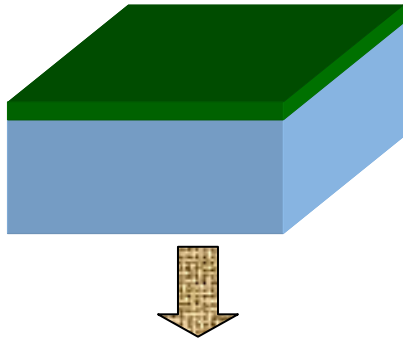
(f) Illustration of the wet etching
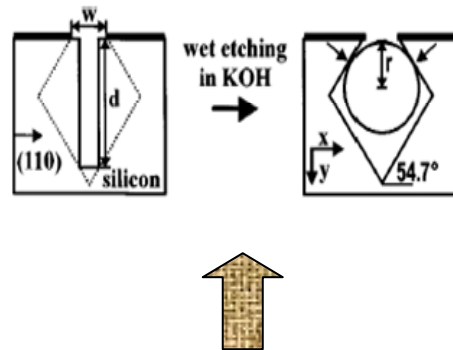
(b) Step 2. Lithography and RIE
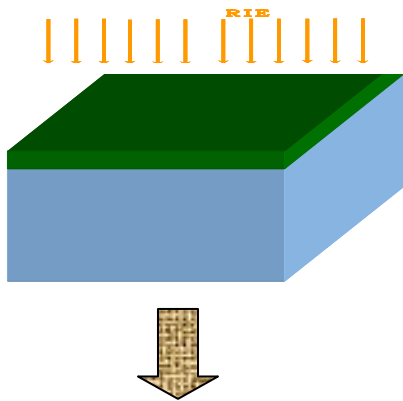
(e) Step 5. Anisotropic wet etching of KOH
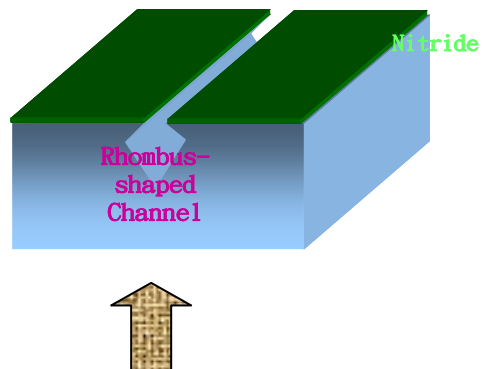
(c) Step 3. Openings on the nitride layer
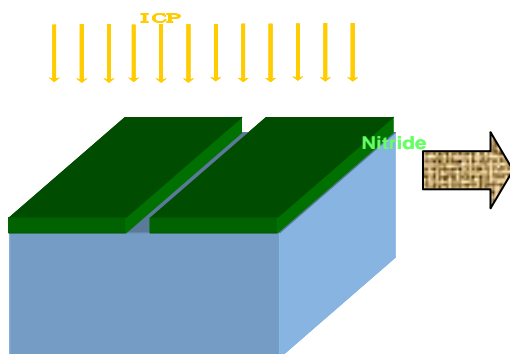
(d) Step 4. Trenches are 158um in depth by ICP etching
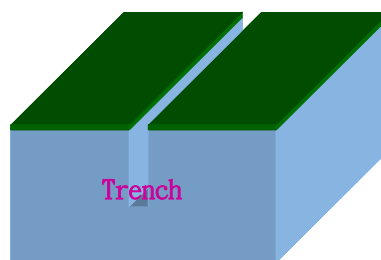
Fig. 4-2 Process flow of the rhombus-shaped channel. (a) 0.5um nitride layer deposited by LPCVD, (b) lithography and RIE, (c) openings on the nitride layer and then ICP etching, (d) trenches are 158um in depth by ICP etching, (e) anisotropic wet etching of KOH, and (f) illustration of the wet etching.

Because the fiber is precisely aligned against the upper {111}-planes of rhombus, the position of the fibers is precisely referenced to the surface of the wafer. The unexpected displacement of the fiberlens in the Rhombus-shaped Channel mainly results from the surface roughness of upper {111}-planes of rhombus.

The SEM photo shown in Fig. 4-3 is the rhombus-shaped channels fabricated in NFC. The width of trenches in our photomask is designed as 70um. The photo shows that the cross-section of our rhombus-shaped channels is not smooth. The smoother end-face is achieved by the dicing saw, and TMAH (20 wt. %, 80°C) with IPA or K_2CO_{3aq} can improve the surface quality.
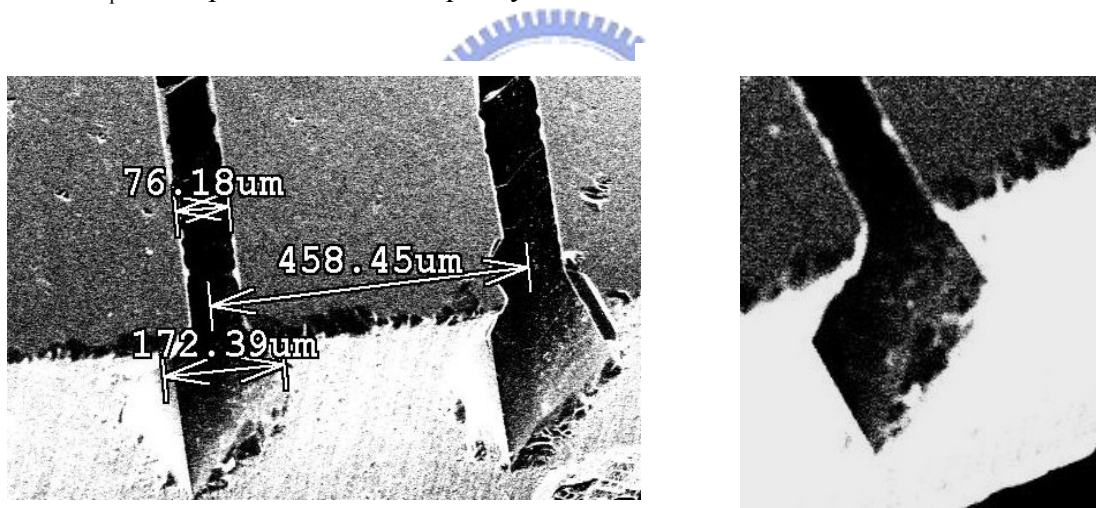
Fig. 4-3 SEM photos of the rhombus-shaped channels

Rhombus-shaped channels simplify the fabrication of multichannel systems. Therefore, they seem to be suitable as ferrules for fibers in micro-optical systems.

4.4 Fabrication of free-space micro-gratings

The free-space integrated optical pickup head is usually fabricated by the micro -hinged technology [1] [2] using the two-layered poly-silicon process. A typical mask design is shown in Fig. 4-4. Fig. 4-5 illustrates the fabrication of vertically free-space hinges. As shown in Fig. 4-5(a), the first polysilicon layer of 2um thickness is deposited on top of sacrificial oxide layer and then patterned using conventional photolithography. Various optical elements such as Fresnel lenses, mirrors and gratings are made in this polysilicon layer using photolithography and dry etching. The hinge-pins are also defined in this polysilicon layer. Then, another sacrificial oxide layer is disposed and the second polysilicon layer of 2um is defined. Finally, by selectively removing the sacrificial oxide layers with HF (etching rate of oxide layer is 1um/min), staples made in the second polysilicon layer can fix the rotatable optical elements around hinges on the first polysilicon layer as shown in Fig. 4-5(b).
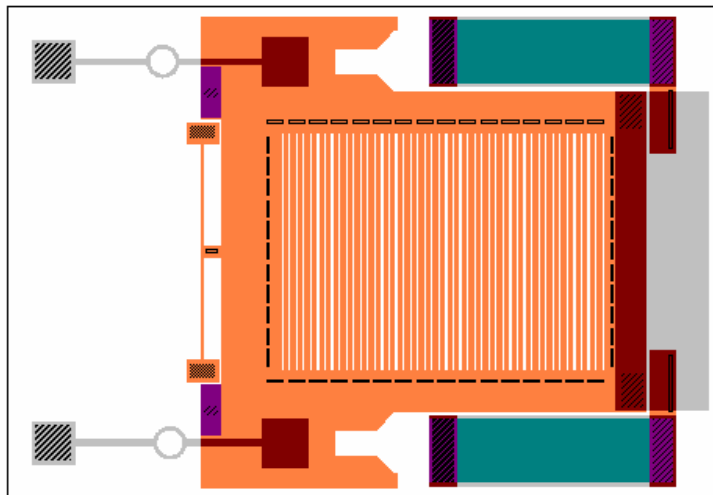
Fig. 4-4 A typical mask design of a micrograting using the two-layered poly-silicon process
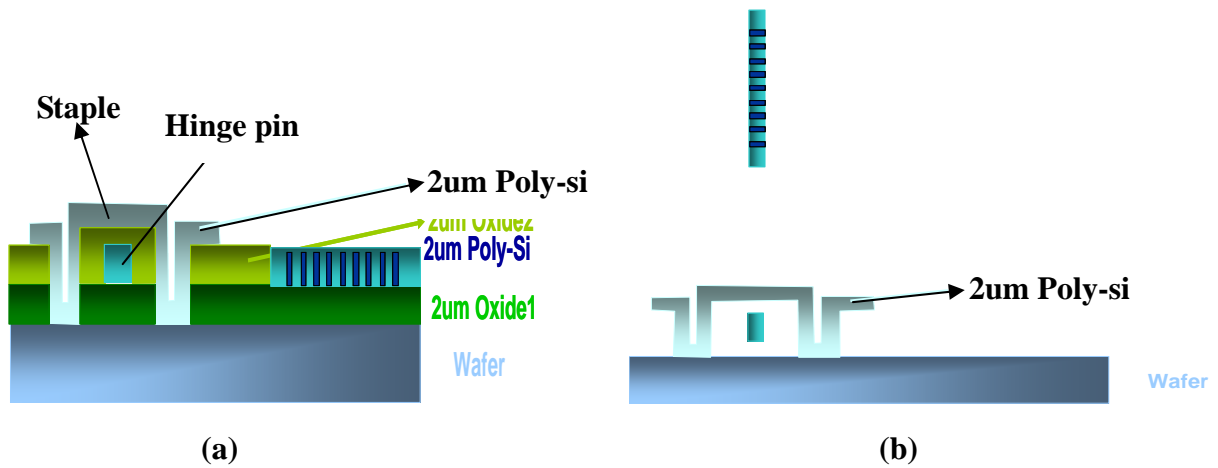
Fig. 4-5 (a) Cross-sectional view illustrated for two-layered poly-silicon technique, and (b) cross-sectional view after release process and being lifted-up.

The above design is based on MUMPS process, and the process with 8 masks is required. To reduce the fabrication complexity, we proposed a simpler process, which require 3 masks only. Instead of poly-silicon, the Si_3N_4 film is used as the structural layer of optical components. Our mask design is shown in Fig. 4-6.
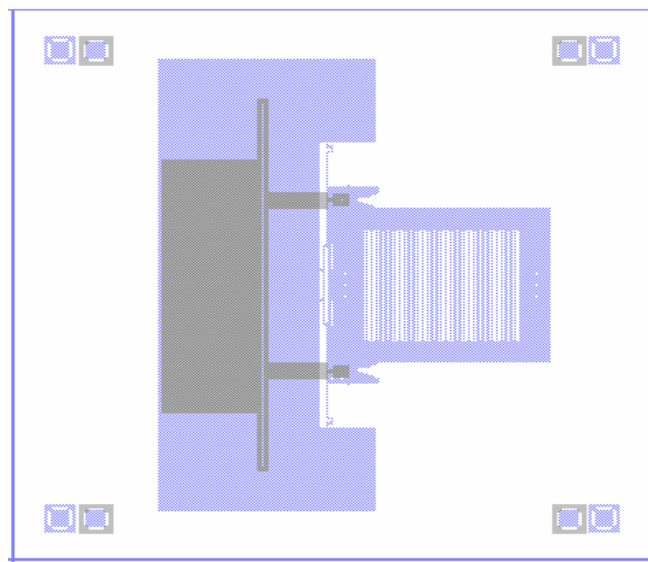
Fig. 4-6 A mask design of a micrograting using the Si_3N_4 film as the structural layer

The schematic of our fabrication flow are shown in Fig. 4-7. First, the nitride layer was patterned for forming the profile of micro-grating on the oxide layer. After the structural and sacrificial layers were deposited, the mechanism for supporting the micro-grating was achieved by RIE. Then the micro-grating was fabricated after the release process. The release process is shown in Table 4-1. Finally, using the mechanism made of poly-silicon to fix the micrograting, an out-of-plane micrograting can be realized by operating a probe through the microscope, as shown in Fig. 4-8.

Table 4-1. Release process. Acetone $\longrightarrow$ IPA $\longrightarrow$ D.I. Water $\longrightarrow$ HF release $\longrightarrow$ $CH_3OH_{a.q.}$ (CH_3OH : water =4:1) $\longrightarrow$ CH_3OH

Solution	Time(minutes)	Function
Acetone	25	Rid of the photoresist
IPA	2	Cleaning
D.I. Water	5	Cleaning
HF	5	Release of the sacrificial layers
$CH_3OH_{a.q.}$	5	Cleaning
CH_3OH	10	Cleaning

(a)

0.75um Si₃N₄
2um SiO₂

Step 1. PECVD 2um oxide and then
LPCVD 0.75um Si₃N₄

RIE

(b)

Step 2. Lithography and then patterning
by RIE

LPCVD

(c)

2um Poly-si
2um SiO₂

Step 3. PECVD 2um oxide and then
LPCVD 2um Poly-silicon

RIE

(d)

Step 4. Lithography and then patterning
by RIE

Release of sacrificial layers

(e)

Step 5. Release process. Acetone
(25 minutes) ⟶ IPA (2 minutes)
Water (5 minutes) ⟶ HF release
(5 minutes) ⟶ CH₃OH_{a.q.} (CH₃OH :
water = 4:1, 5 minutes) ⟶ CH₃OH
(10 minutes)

(f)

CO$_2$ dryer

Step 6. Drying by CO$_2$ dryer

Fig. 4-7 Fabrication flow of the out-of-plane micrograting with a self-engaging locking mechanism. (a) PECVD 2um oxide and then LPCVD 0.75um Si$_3$N$_4$, (b) lithography and then patterning by RIE, (c) PECVD 2um oxide and then LPCVD 2um Poly-silicon, (d) lithography and then patterning by RIE, (e) release process, and (f) drying by CO$_2$ dryer
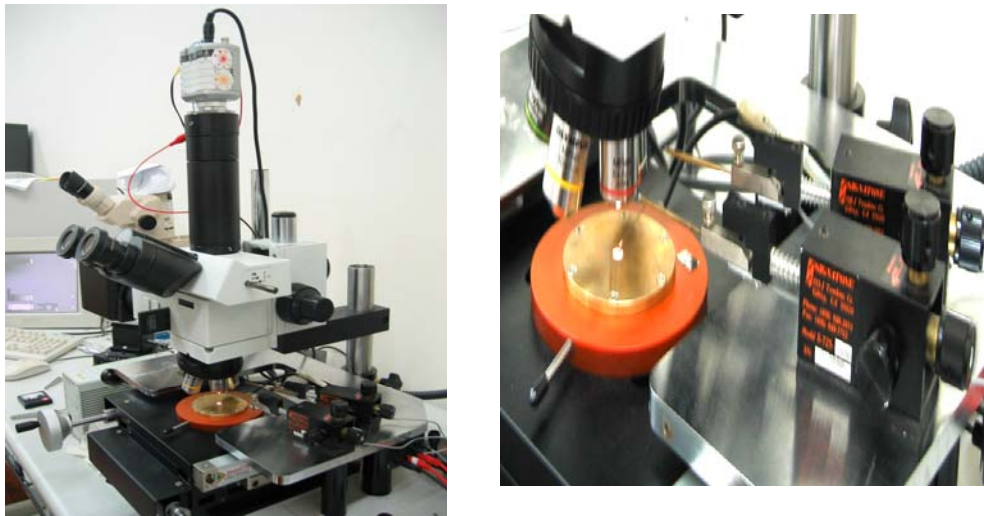
Fig. 4-8 Photos of the probe system

In order to improve the stability and angular alignment, the frame of grating is held in place with a self-engaging locking mechanism. As shown in Fig. 4-9(a), the lock consists of a tether made of poly-silicon, and a keyhole opening in the frame of grating. When the frame of grating rotated to the designed angle, the tether slides into the keyhole and locks the frame of grating. As shown in Fig. 4-9, the assembly of

out-of-plane micrograting was illustrated. As shown in Fig. 4-10, the out-of-plane

micrograting was held with the self-engaging locking mechanism.

(a)　　　　　　　　　　　　　　(b)

(c)　　　　　　　　　　　　　　(d)
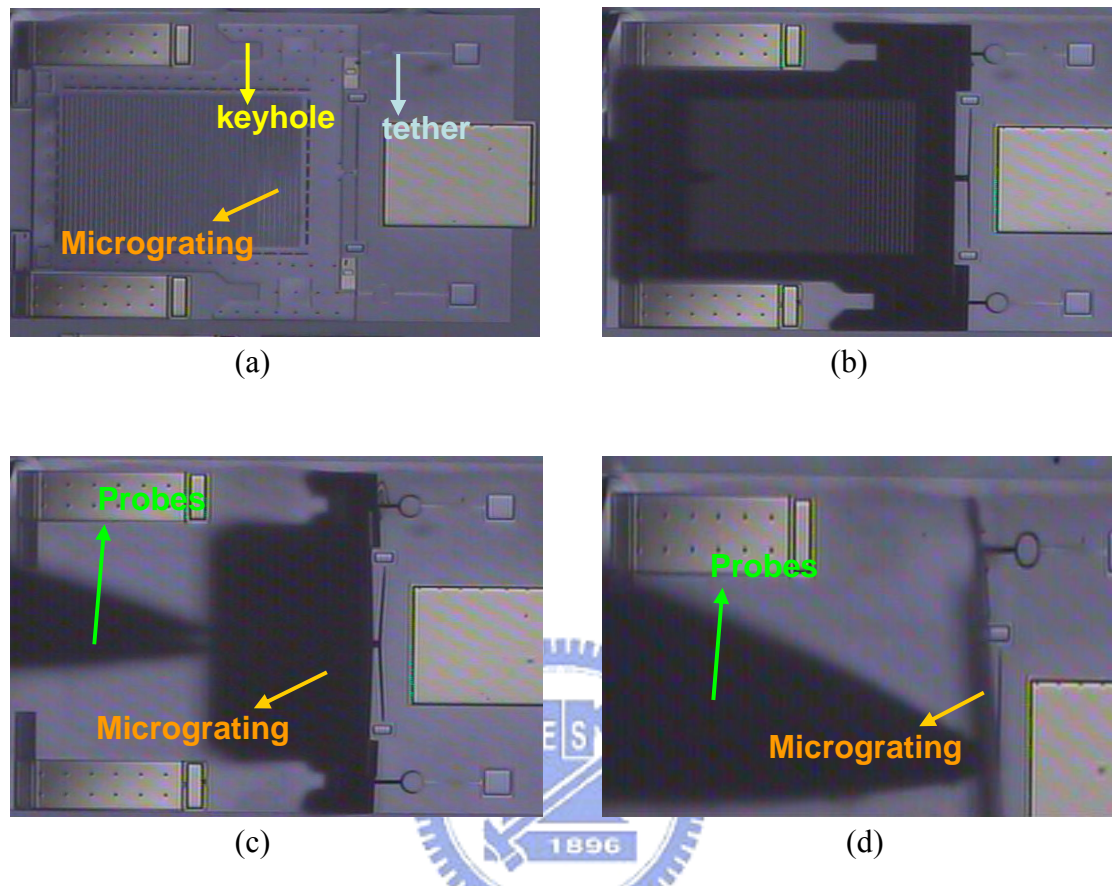
Fig. 4-9 Flow of the assembly of out-of-plane micrograting. Under the microscope, a
probe was used to rotate the micrograting out of the substrate, as shown in (a), (b), (c),
and (d).

Fig. 4-10 Under the microscope, the out-of-plane micrograting was held with a
self-engaging locking mechanism

4.5 Future work of equivalent blazed microgratings

Generally, optical property of blazed gratings is better than rectangular gratings with equal filling-factor. However, it is difficult to fabricate blazed microgratings. Therefore, blazed microgratings are not yet adopted in our current optical system.

Instead of changing the micrograting thickness, it is possible to keep the thickness fixed, while linearly changing the refractive indices, namely, realizing an equivalent blazed micrograting with isosceles triangle shapes. Linearly changing the filling factor of microgratings with equal difference, an equivalent blazed grating will be developed by the E-beam Writer in NDL, as shown in Fig. 4-11. After the dry etching, an equivalently blazed grating made of Si_3N_4 will be realized.
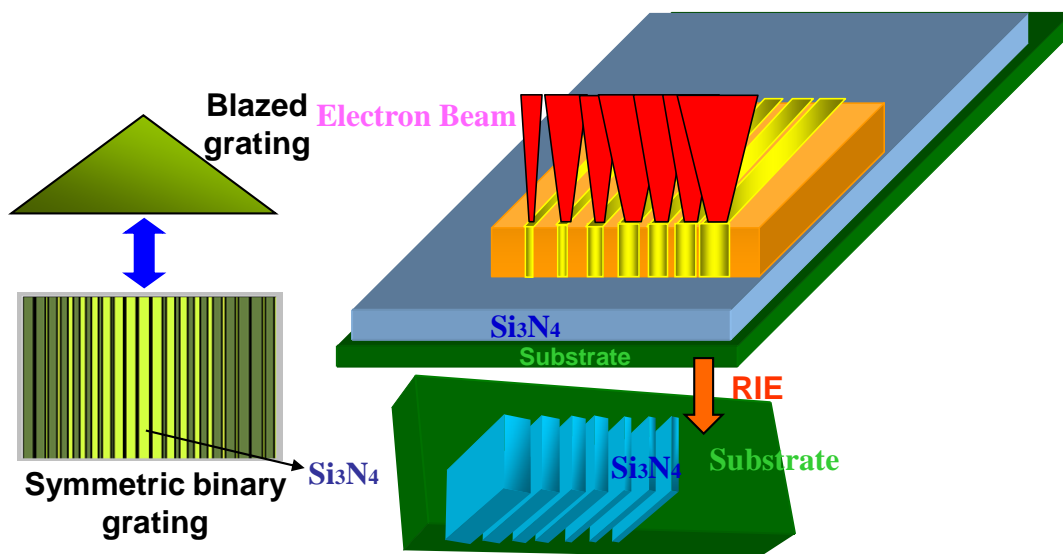
Fig. 4-11 Schematic of the equivalent blazed grating

From the GSOLVER simulation of the equivalent blazed micrograting, contrast to rectangular gratings with equal filling factor, the diffraction efficiency of the zeroth and two first orders beams is improved, and the diffraction angle between the zeroth and two first orders is smaller. Diffraction efficiency distribution of microgratings is

more suitable for pickup-head system, when the difference of filling factor is smaller. Due to the limitation of the GSOLVER, we still can not evaluate optimal difference of the filling factor. Besides, it is difficult to fabricate finer grating ridges with properties close to subwavelength gratings. One is to use E-beam writing. But the E-beam writter in NDL is only applied to 6 inches wafers, and therefore out of accordance with the MOEMS process in NFC. Expectantly, equivalent blazed gratings will be realized in the near future.

4.6 Summary

The fabrication of the rhombus-shaped channels and free-space microgratings was presented in this chapter. The fiber-alignment structures of rhombus-shaped channels can provide the fiber system with precise optical-axis position. According to the demonstration of the feasibility of the process, optical components such as free-space microgratings are achieved by the residual sacrificial layers as fixation to the substrate, and the self-engaging locking mechanisms. Therefore, all free-space optical components of our pickup-head system will be realized in the near future.

Chapter 5

Measurement

5.1 Introduction

According to the fabricated results described in Chapter 4, the measurement results will be shown in this chapter. Optical measurement of the fiberlens operating in the 405nm spectrum and the diffracted beams of the micrograting will be shown. As the beam-shaping components, spot images from the fiberlens must be measured to assure the collimated throughput and examine their spot size. The diffraction efficiency and angle of our micrograting were evaluated to examine fabricated components to serve our purpose for the pickup-head. Besides, we calculated the coefficients of Seidal aberration to explore the potential issues of the incident beam on the grating. Finally, the evaluation of measurement results will be discussed.

5.2 Optical measurement of the fiberlens operating in 405nm spectrum

For evaluating the quality of the spot images from the fiberlens operating in the 405nm spectrum, these spot images must be magnified because the spot size is in the order of micrometers. The measurement setup consists of a blue laser source, magnification 10X and 50X (Olympus 50X magnification, NA = 0.75, f = 180) objective lenses, a three-axis (x-y-z) fiber coupler, the SMF (single-mode-fiber) with a fiberlens, two-axis (x-z) stages, attenuators (ND-filters), a CCD camera, and an IMAQ card, as shown in Fig. 5-1. The spot diagram and energy distribution can be

51

measured by this optical system, and further analyzed by the Matlab software. All these measurement components were fixed on an optical bench to maintain the alignment along the optical axis. The intensity and wavelength of the blue-laser source (GaN semiconductor laser) is 4 mW and 405 nm, respectively. The SMF is 125 μm in diameter, and 5 μm in core diameter, whereas the hemispherical microlens, called fiberlens, fabricated on the front-end of the SMF is 62.5 μm in radius and has the same refractive index as the core of the SMF.

In this measurement system, the NA of objective lens must be larger than the one of the fiberlens, so that the beam from the fiberlens can be transmitted completely to the CCD camera without huge loss. Besides, the NA of objective lens must be large enough to provide sufficient resolution ability for the focused spot of the fiberlens. The ND-filters are used to reduce the light-intensity of the blue-laser captured by CCD pixels for avoiding the CCD pixels to be saturated due to the concentrative energy -density. But the interference between these ND-filters results in the noise. Besides, these ND-filters do not have any polarization, dispersion, and non-uniform attenuation.

Using the CCD camera and IMAQ card, the intensity-distribution of captured images can be digitalized and analyzed by the Matlab software. But the intensity-distribution of digitalized spot images is not very accurate, because some data of images may not be detected due to the limitation of the sensitivity of CCD pixels. However, contrast to the knife-edge-method and pin-hole-method, digitalized image-capturing seems to be convenient for measuring the spot size.
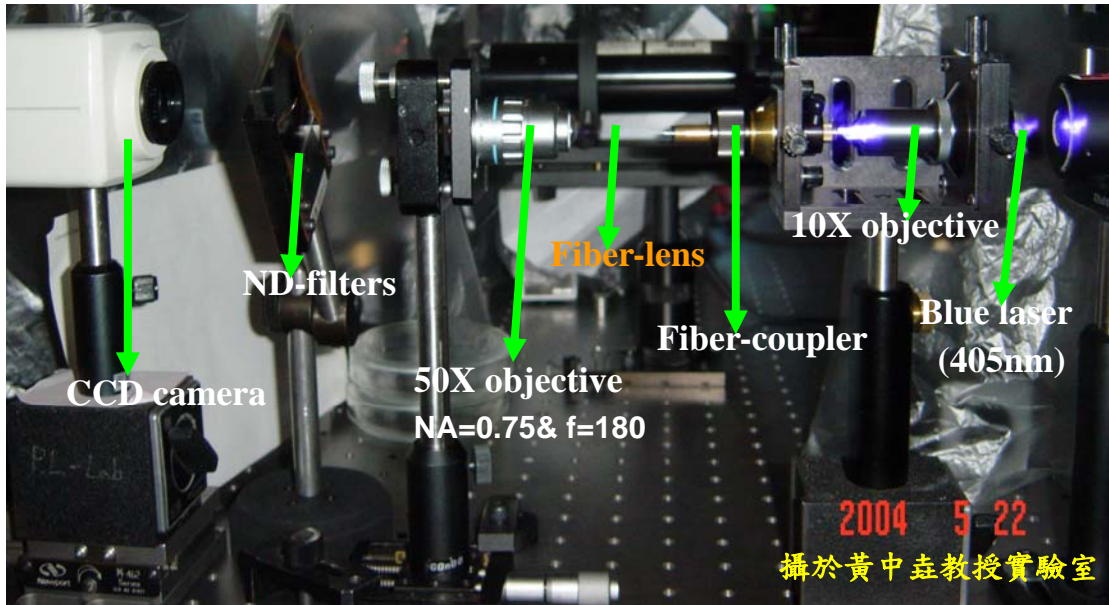
Fig. 5-1 Optical measurement system of the fiberlens.
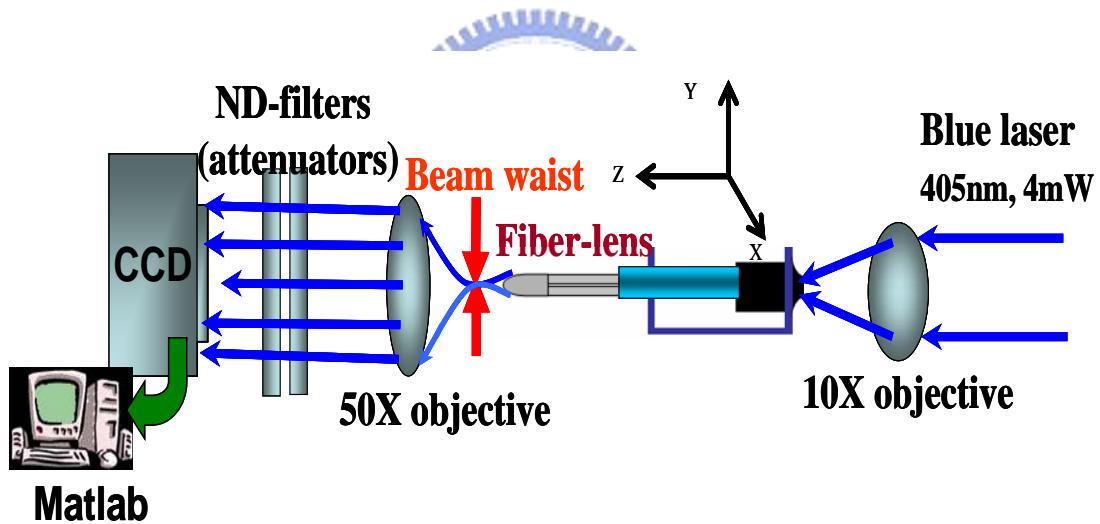
Fig. 5-2 Schematic of the measurement system of the fiberlens

The schematic of optical measurement system was shown in Fig. 5-2. We adjusted the relative distance of the objective lens (10X) and the coupler until coupling the blue-laser beam into the SMF by the objective lens (10X), where the cross-section of the SMF must be smooth. The SMF with a fiberlens was mounted on the XYZ three-axis coupler. The position of the beam waist of the fiberlens must be

53

just situated in the focal plane of the objective lens (50X), so that the smallest spot images at the beam waist can be detected by the CCD camera. The size of spot images (full-width at half maximum) can be measured by calculating the number of CCD pixels covered in the spot. We selected the length of the silica rod to achieve the fiberlens with suitable focal length, since the distance between the fiberlens and the micrograting was 500um in our system. Considering the aberration and additional other components between the fiberlens and the micrograting, we chose the silica rod of 400um. The measurement results shows that the spot size at the beam-waist is 7um, when the length of the silica rod is 400um and focal length is 250um, as shown in Fig. 5-3.
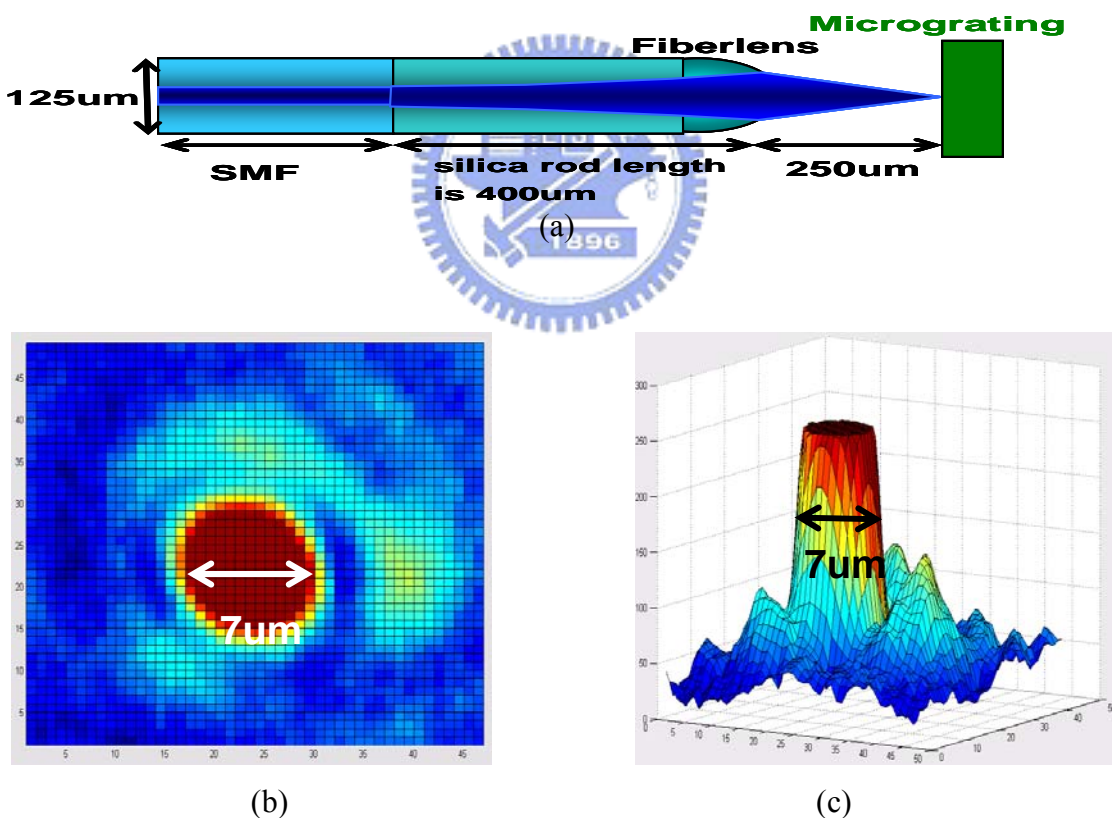
Fig. 5-3 (a) The fiberlens is used as a collimator, where the length of the silica rod is 400um and focal length is 250um, (b) the 2D-pcolor diagram of the spot image at the beam waist analyzed by the Matlab, and (c) the 3D-surface diagram of the spot image at the beam waist analyzed by the Matlab.

5.3 Optical measurement of the micrograting

The diffraction efficiency and angle of micrograting were measured by the optical microscope (Nikon Eclipse E600) with digital-control micro-displacement system, as shown in Fig. 5-4. The blue laser from an outside laser source was reflected by the mirror. The beam size was reduced by the condenser (f = 0.5cm), then incident on the micro-grating in the stage of the optical microscope. By the micro-displacement system, the micrograting can be adjusted on the optical-axis. The micrograting is just located in the focal plane of the 10X objective lens, so that the splitting three-beams are expanded by the objective and measured by the CCD camera.

The diffraction efficiency ratio and angle of the three beams can be achieved by the Matlab software, as shown in Fig. 5-5. The diffraction angles is Arctan (1.56/30) = 2.98° , where the distance between the objective and CCD pixels is 30cm, and the zeroth and the ±1 orders beams is 1.56cm according to the number of CCD pixels. The diffraction-angles nearly matches the ideal value of 2.9° derived from the grating equation. The diffraction efficiency ratio between the zeroth order and the two first orders beams is about 5, but the ratio is still too small.

.

Fig. 5-4 The schematic of the measurement system of the microgratings

(a)

(b)
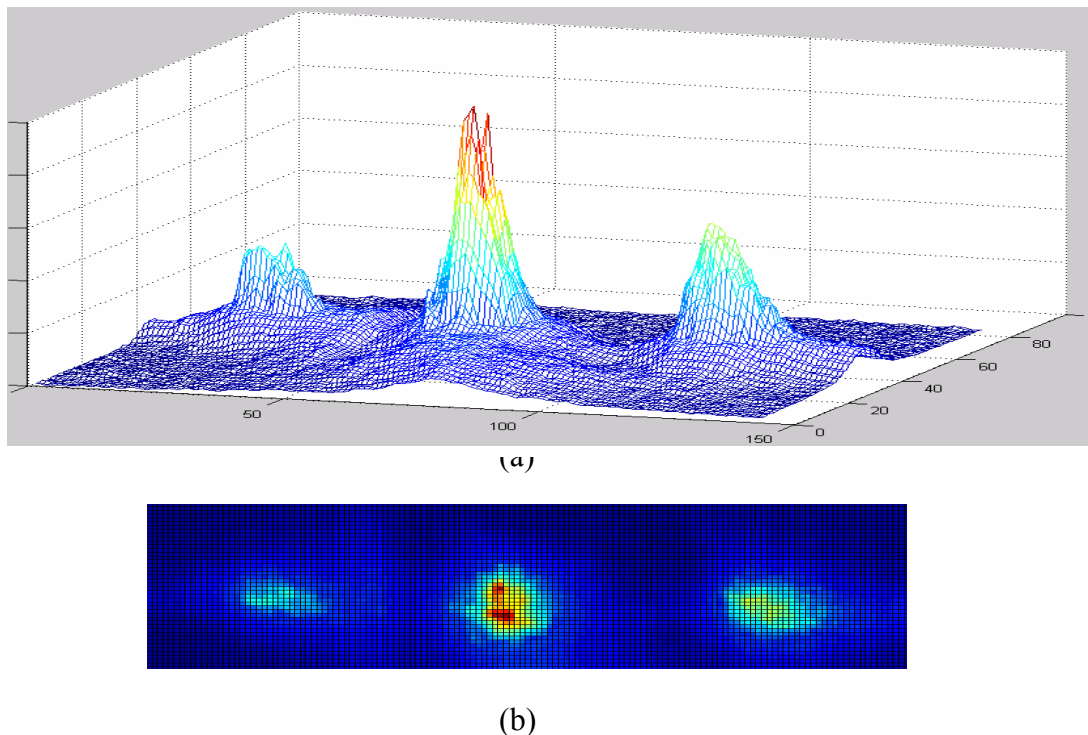
Fig. 5-5 (a) Diffraction efficiency distribution of our microgratings (period=8um). The ratio between the zeroth order and the ±1orders beams is about 5, and (b) the spot images of diffracted beams, including the zeroth order and the ±1 orders beams.

5.4 Evaluation of spherical coefficient W$_{040}$ of the fiberlens

Because the optical pickup-head is not an imaging system, the shape of spot images is not very important, so the field curvature and distortion can be ignored. Since the fiberlens is located a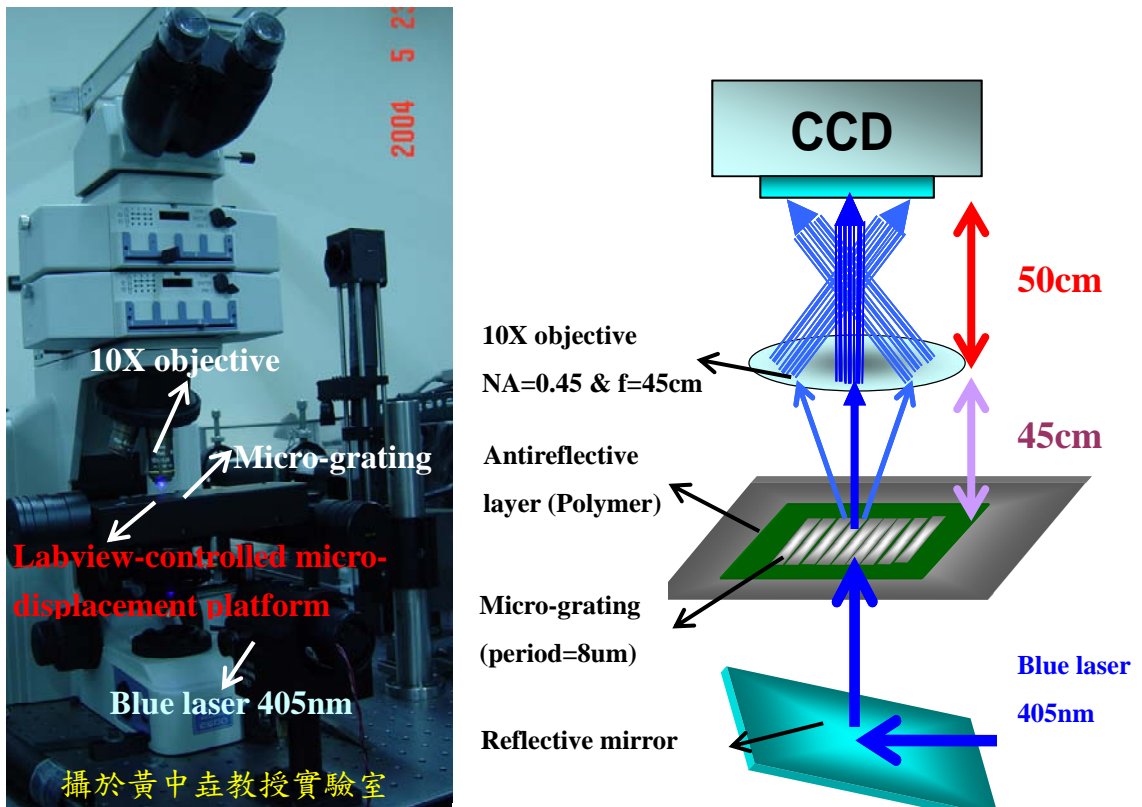long the optical-axis, the coma and astigmatism are negligible. Therefore, the quality of spot images from the fiberlens is mainly determined by the on-axis spherical aberration. The coefficients of Seidal aberration of measured spot images, especially the spherical coefficient W$_{040}$, can be really achieved according to the comparison with a series of simulated image diagrams by the Matlab, as shown in Figs. 5-6, 5-7, 5-8, and 5-9, where their xy-plane represents the position of CCD pixels, and the value of their z-axis is normalized light-intensity. We only showed the spot images with the spherical coefficients W$_{040}$= 0 and 0.4. With the value of W$_{040}$ increases, the spot size becomes larger. These simulated image diagrams were plotted according to the spherical aberration polynomial shown in Equation 5-1.

$$W(\rho,\phi) = W_{040}(\frac{\rho}{NA})^4 \qquad\qquad \textbf{Eq.5-1}$$

, where $\quad \rho,\phi) = (\sqrt{\sigma_x^2 + \sigma_y^2}, \tan(\frac{\sigma_y}{\sigma_x}));0 \le \rho \le NA$

, W$_{040}$ is the spherical aberration coefficient, and its initial value can be evaluated by optical software such as OSLO, NA is the numeric aperture of the fiberlens, and σ_x, σ_y, ρ, Φ are variables in the polar coordinate.

By this method, the experimental aberration of the fiberlens can be evaluated precisely. It is helpful to inspect the optical quality of components, since the aberration of incident beams is identified.
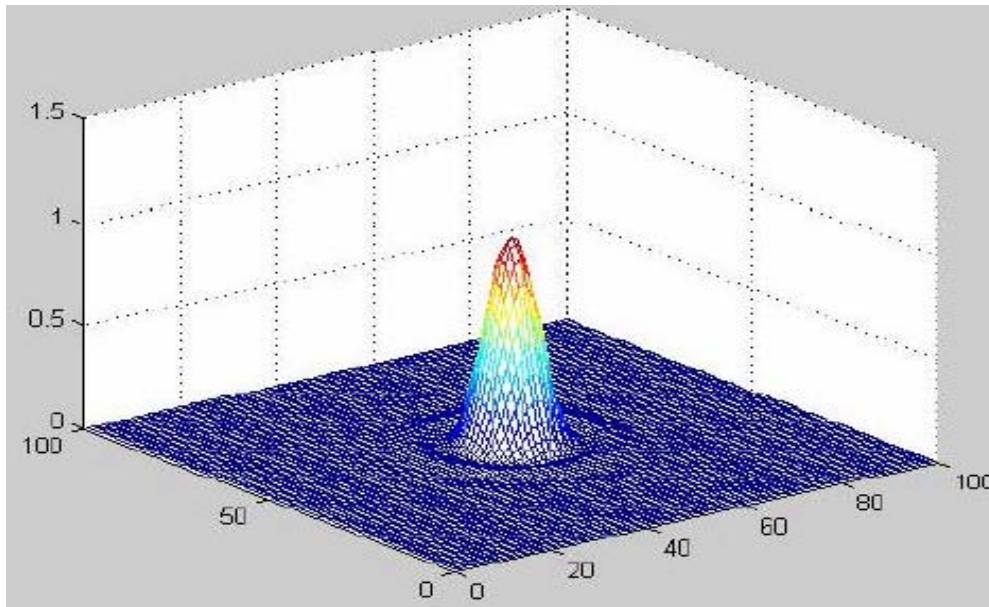
Fig. 5-6 The 3D-mesh diagram of the spot image without the aberration. The diagram is plotted by the Matlab software, where the xy-plane represents the position of CCD pixels, and the value of the z-axis is normalized light-intensity.
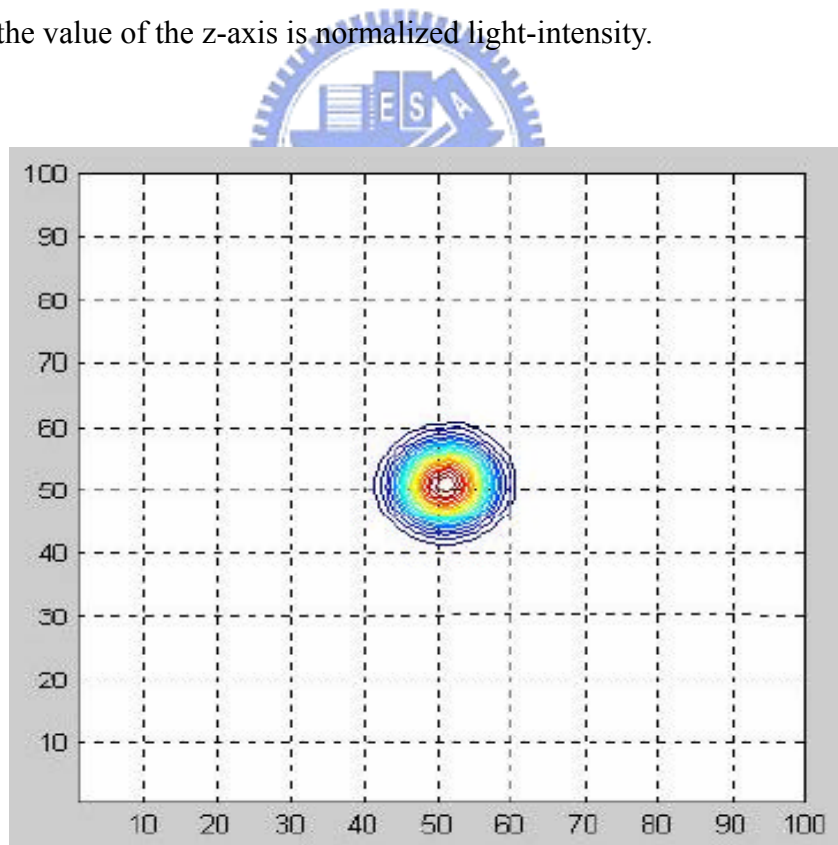
Fig. 5-7 The 2D-contour diagram of the spot image without the aberration. The diagram is plotted by the Matlab software, where the xy-plane represents the position of CCD pixels.
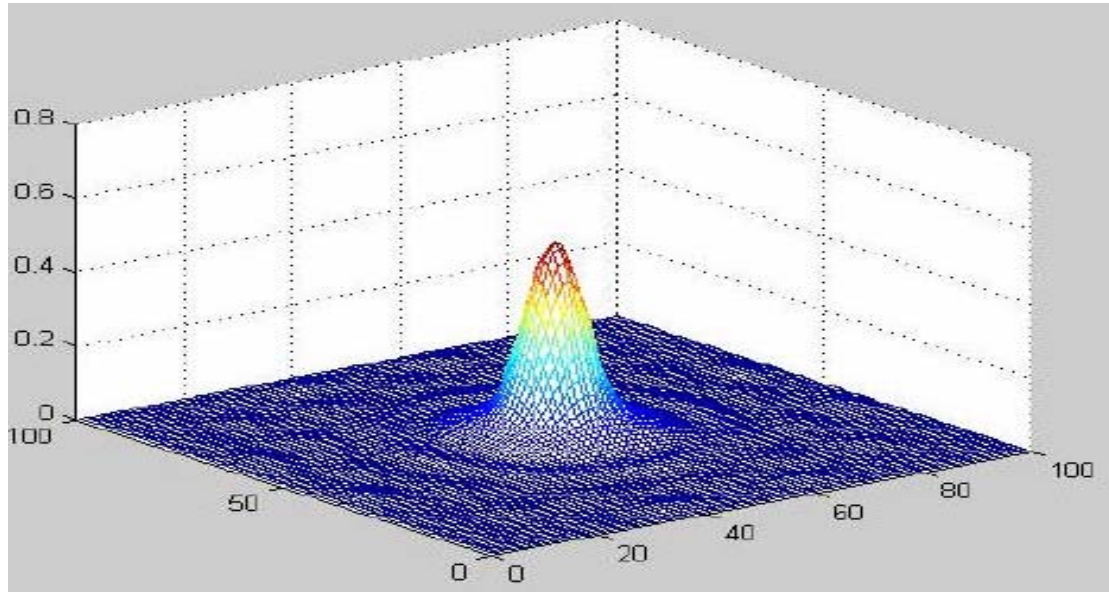
Fig. 5-8 The ideal 3D-mesh diagram of the spot image with the spherical coefficients $W_{040}=0.4$. The diagram is plotted by the Matlab software according to the Zernike's polynomial, where the xy-plane represents the position of CCD pixels, and the value of the z-axis is normalized light-intensity.
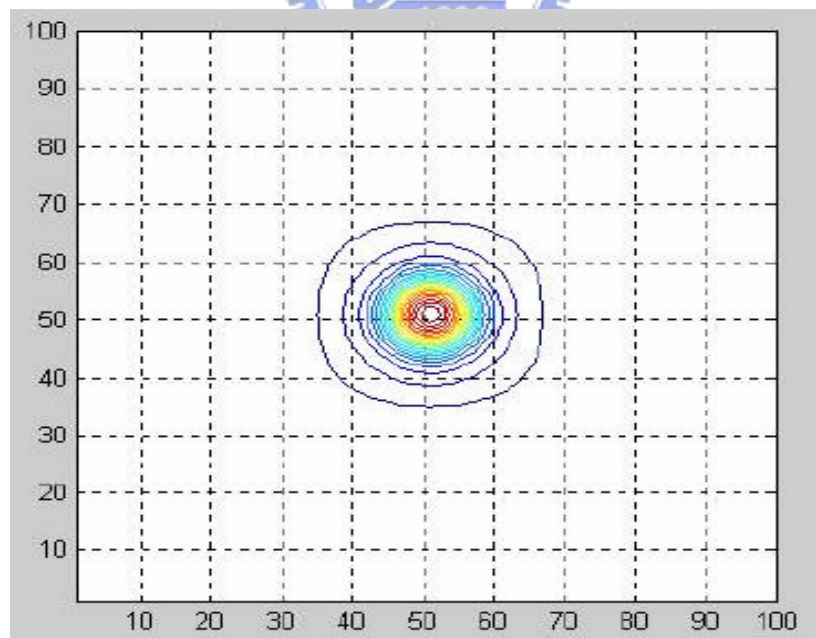
Fig. 5-9 The ideal 2D-contour diagram of the spot image with the spherical coefficients $W_{040}=0.4$. The diagram is plotted by the Matlab software according to the Zernike's polynomial, where the xy-plane represents the position of CCD pixels

5.5 Disscussion of measurement results

The diffraction efficiency ratio between the zeroth order and two first orders is about 5, while the simulated results show that the ratio-values are from 6 to 12. The deviation of energy distribution and light-efficiency of three beams may result from the process quality of the micrograting. The roughness and period of our micrograting are analyzed according to the AFM photographs, as shown in Figs. 5-10 and 5-11. The roughness of micrograting ridges without the release process is the order of 10~20 nm. The length of one ridge is about 3.28um, representing the filling factor is 0.41. According to the Fig. 3-5, the filling factor of 0.41 is located in the periphery of target region (green region), and additionally the micrograting thickness is 0.78um~0.8um instead of the simulated results of 0.75um, therefore, the diffraction efficiency ratio is necessarily low. Besides, the diffraction efficiency of the +1 order and the -1 order beams are not equal, the deviation may result from the asymmetrical trapezoid -shaped ridges, the non-uniformity of the micrograting thickness, and even cracks or corrugation.

On the other hand, since our optical components are made of thick Si_3N_4 (thickness $\geq$ 0.3um), they tend to have serious cracks and rough surface, as shown in Fig.5-12, and therefore the yield of components is low.

The spot size of incident beam must cover plenty ridges to enable the micrograting to function diffraction. Generally, the number of ridges covered in the spot must be 12 at least. Obviously, the beam from the fiberlens is too small, and therefore a micro beam-expandor with high efficiency is required. To date, additional GRIN fiber module seems to be one solution.

Peak Surface Area Summit Zero Crossing Stopband Execute Cursor

Roughness Analysis

30.0

20.0

Image Statistics

Img. Z range	2.578 µm
Img. Mean	0.041 nm
Img. Raw mean	-16.050 nm
Img. Rms (Rq)	793.17 nm
Img. Ra	713.04 nm

Box Statistics

Z range	150.88 nm
Mean	654.27 nm
Raw mean	730.86 nm
Rms (Rq)	12.940 nm
Mean roughness (Ra)	9.946 nm
Box x dimension	1.875 µm
Box y dimension	28.828 µm

10.0

0

0   10.0   20.0   30.0 µm

bounds.177

Peak On   Summit Off   Zero Cross. Off Box Cursor

Fig. 5-10 AFM photograph of the roughness of the micrograting. The R_{rms} of the roughness is 12.94nm.

Cursor Marker Spectrum Zoom Center Line Offset Clear

Section Analysis

nm

1000

0

-1000

0   10.0   20.0

µm

L	3.281 µm
RMS	12.813 nm
lc	DC
Ra(lc)	5.391 nm
Rmax	27.313 nm
Rz	16.774 nm
Rz Cnt	valid
Radius	27.518 µm
Sigma	14.116 nm

Spectrum

Surface distance	3.288 µm
Horiz distance(L)	3.281 µm
Vert distance	27.313 nm
Angle	0.477 °
Surface distance	
Horiz distance	
Vert distance	
Angle	
Surface distance	
Horiz distance	
Vert distance	
Angle	
Spectral period	DC
Spectral freq	0 Hz
Spectral RMS amp	0.031 nm

DC   Min

bounds.177

Cursor: fixed   Zoom: 1:1   Cen line: Off   Offset: Off

Fig. 5-11 AFM photograph of the profile of the micrograting without the release process. The ridge length of the micrograting is 3.28um

61
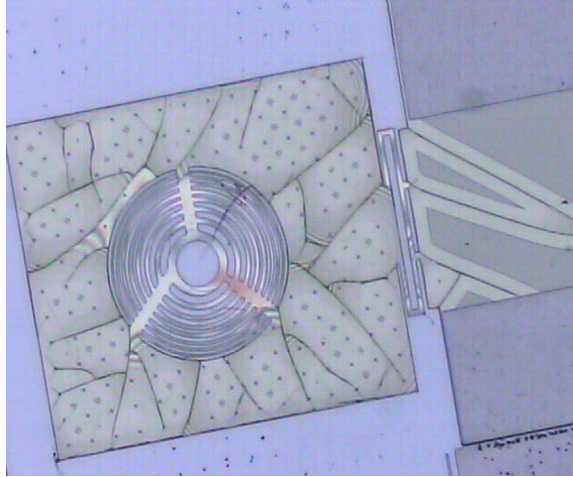
Fig. 5-12 Optical components made of thick Si_3N_4 layers tend to have serious cracks and rough surface.

5.6 Summary

Considering additional beam-expandor being required between the fiberlens and the micrograting, we chose the fiberlens module with the silica rod of 400um as the beam-shaping component. Its spot size at the beam-waist is 7um, and focal length is 250um. Diffraction efficiency of our microgratings is not high expectedly due to the process error, especially the asymmetrical trapezoid-shaped 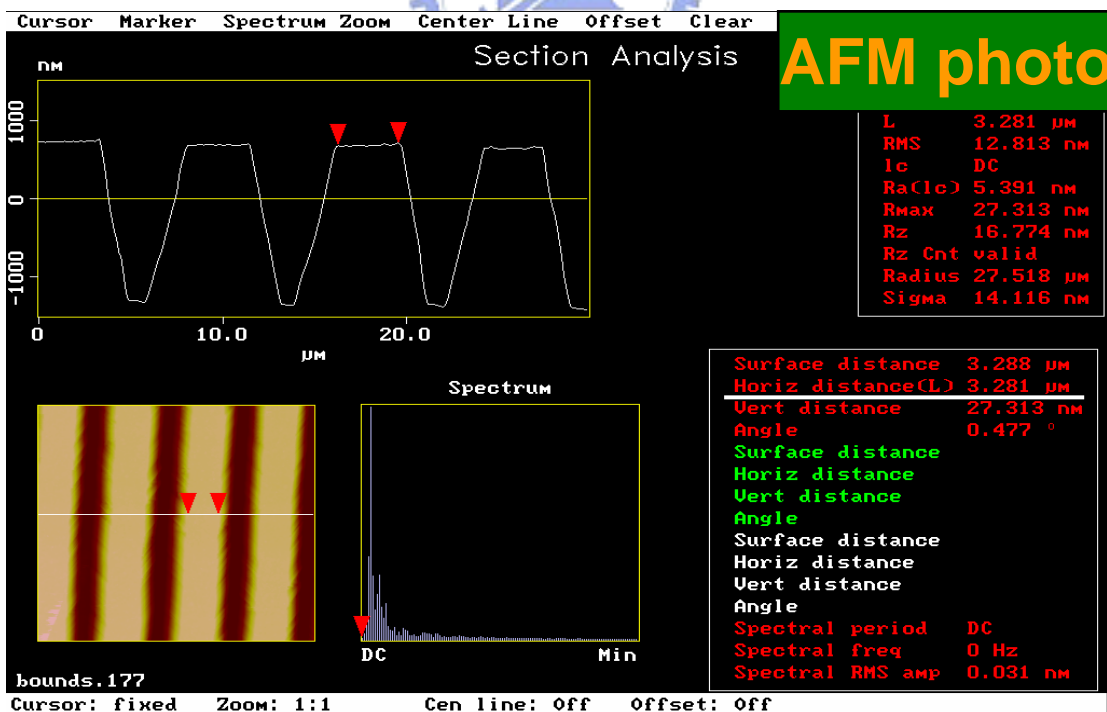grating ridges instead of rectangular shape. Since these process issues affect the optical performance of our micrograting, obviously, the process tolerance considered in advance is necessary. Therefore, the fabricated samples still serve our initial design target.

Chapter 6

Conclusion

We used the beam-shaping component of the fiberlens to guide the blue-laser beam into the free-space micro-pickup-head system. The fiber-alignment structures of rhombus-shaped channels were used to hold the fiberlens precisely. The free-space micrograting separated the incident beam into three beams for the tracking error detection.

The rhombus shaped channels were achieved by the dry etching of RIE and ICP, and wet etching of KOH. For inserting the fiber into the rhombus-shaped channel, the depth and width of the trench must be larger than 125um and 64.5um. The fiberlens height represents the optical-axis height, and can be precisely examined by measuring the width of the opening on the top surface of rhombus-shaped channels. Therefore, the optical-axis height of micro-pickup-heads can be controlled reliably by adjusting the shape and size of the rhombus.

We chose the silica rod of 400um to achieve the fiberlens with suitable focal length of 250um, and its spot size at the beam waist was 7um, since the distance between the fiberlens and the micrograting was 500um in our system, and a beam-expandor was required between the fiberlens and the micrograting. However, the spot size of incident beam must cover plenty ridges to enable the microgratings to function diffraction. Generally, the number of ridges covered in the spot must be 12 at least. Obviously, the beam from the fiberlens is too small, and therefore a micro

beam-expandor with high efficiency is required. To date, adding the GRIN fiber module between the SMF and fiberlens seems to be one solution

Our free-space micrograting is made of low-stress Si-rich-Si$_3$N$_4$ deposited by LPCVD, since the nitride has high transmission efficiency in the blue-laser spectrum. To achieve the expected diffractive efficiency distribution of the zeroth and two first orders beams (-1 order: 0 order: +1order = 1 : 6~12 : 1), the period, depth, and filling factor of our free-space micrograting were 8$\pm$0.25um, 0.75$\pm$0.05um, 0.5$\pm$0.1 according to the GSOLVER simulation. With the MOEMS technology, the free-space micrograting were achieved by the self-engaging locking mechanisms, and the residual sacrificial layers as fixation to the substrate. The diffraction efficiency ratio between the zeroth order and two first orders was about 5, but this value was not high as the simulated results due to the process error, especially trapezoid-shaped grating ridges instead of rectangular shape. Since the process tolerance was considered in advance, the fabricated samples still serve our initial design objective.

Great efforts are needed to realize the free-space micro-pickup-head systems. The main issue of gratings is to enhance diffraction efficiency and to reduce diffraction angle, since the data density become more compact in the next-generation storage system. The multi-step diffractive optical elements or equivalent blazed gratings are being developed to improve diffraction efficiency of 3 beams up to 90% at least, and to make diffraction angle less than 1° .With the demonstration of the feasibility of free-space optical components, free-space pickup-head elements will be realized in the near future.

References

Chapter 1

[1] P. N. Prasad, Introduction to Bio-photonics, Johnwiley & Sons, New Jersey, (2003)

[2] S. Kwon, L. P. Lee. Stacked two dimensional micro-lens scanner for micro confocal imaging array, Micro Electro Mechanical Systems, 2002. The 15th IEEE International Conference, 20-24 (2002)

[3] L. J. Hornbeck, Digital light processing for high-brightness high-resolution applications, Proc. SPIE 3013, Electronic Imaging, EI '97; Projection DisplaysⅢ, San Jose, CA, USA, 27-40 (1997) (http: // www.dlp.com)

[4] C. S. E. Miller, Integrated Optics: An Introduction, Bell Systems Technology Journal, Vol. 48, No. 7, 2059-68 (1969)

[5] K. E. Petersen, Silicon as a Mechanical Material, Proc. IEEE, Vol. 70, No. 5, 420-57 (1982)

[6] L. J. Hornbeck, Deformable-Mirror Spatial Light Modulators, Proc. SPIE, Vol. 1150, 86-102 (1990)

[7] M. T. Ching et al., Microfabricated Optical Choppers, Proc. SPIE, Vol. 1992, 40-46 (1993)

[8] K. S. J. Pister et al, Microfabricated Hinges, Sensors and Actuators A, Vol. 33, 249-56 (1992)

[9] T. Shiono et al., Planer-Optic-Disk Pickup with Diffractive Micro-optics, Applied Optics, Vol. 33, 73-50 (1986)

[10] K. Iga, M. Oikawa, S. Misawa, J. Banno and Y. Kokubun, Stacked planar optics: an application of the planar microlens, Appl. Opt. 21 (1982)

[11] C. C. Lee, Y. C. Chang, C. M. Wang, J. Y. Chang, and G. C. Chi, Silicon-based transmissive diffractive optical element, Optics Letters, Vol. 28, #14, 1260 (2003)

[12] L. Y. Lin, J. L. Shen, S. S. Lee and M. C. Wu: Opt. Lett. Vol. 21, 155 (1996).

[13] L.Y. Lin et al., Micromachined Three-Dimensional Micro-optics for Integrated Free-Space Optical System, IEEE Photonics Tech. Lett., Vol. 6, No.12, 1445-47 (1994)

[14] S. S. Lee et al., An 8*1 Micro-Fresnel Lens Array for Free-Space Optical Interconnect, IEEE Lasers and Electro-Optic Society, 1994 Annual Meeting, Boston, Mass., Oct. 31-Nov. 3, (1994)

Chapter 2

Fiberlens:

[1] T. Tschudi and L. Wang, Diffractive optics for semiconductor lasers, in Diffractive optics for industrial and commercial applications, J. Turunen and F. Wyrowski (eds), Akademine Verlag, Berlin, Germany, 217-241 (1997)

[2] S. Sinzinger, K.-H. Brenner, J. Moisel, T. Spick and M. Testorf, Astigmatic gradient-index elements for laser diode collimation and beam shaping, Appl. Opt. 34, 6626-6632 (1995)

[3] L. Cohen and M. Schneider: Appl. Opt. 13, 89 (1974).

[4] C. Edwards, H. Presby and C. Dragone: J. Lightwave Technol. 11, 252 (1993).

[5] K. S. Lee and F. S. Barnes: Appl. Opt. 24, 3134(1985).

[6] G. Eisenstein and D. Vitello: Appl. Opt. 21, 3470(1982).

[7] H. Sakaguchi, N. Seki and S. Yamamoto: Electron. Lett. 17, 425(1981).

[8] J. I. Yamada, Y. Murakami, J. I. Sakai and T. Kimura: IEEE J. Quant. Electron. 16, 1067 (1980).

[9] Chung-Hao Tien, Yi Chiu, and Han-Ping D. Shieh, Light Guiding and Micro-Optical components for High Density Optical Storage Applications, (2003)

[10] D. Marcuse: Bell Syst. Tech. J. 56, 703 (1976).

[11] Mark P. Davidson, "A modal model for diffraction gratings", (2002)

[12] M. G. Moharam, Eric B. Grann, and Drew A. Pommet, Formulation for stable and efficient implementation of the rigorous coupled-wave analysis of binary gratings J. Opt. Soc. Am. A, Vol. 12, No. 5, (1995)

Chapter 3

[1] 李正中, 薄膜光學與鍍膜技術

Chapter 4

Fabrication of the fiberlens:

[1] Chung-Hao Tien, Yi Chiu, and Han-Ping D. Shieh, Light Guiding and Micro-Optical components for High Density Optical Storage Applications, (2003)

Rhombus-shaped channels:

[1] S. A. Bailey, C. A. Jones, M. W. Nield, K. Cooper, I. P. Hall, and A. C. Thurlow, "Recent advances in fiber-to-fiber and fiber-to-waveguide interconnect technology," Int. J. Optoelectron., vol. 9, no. 2, 171-177 (1994)

[2] Y. Hibino, F. Hanawa, H. Nakagome, M. Ishii, and N. Takato, High reliability optical splitters composed of silica-based planar lightwave circuit, J. Lightwave Technol., vol. 13, 1728-1735 (1995)

[3] C. Strandman and Y. Backlund, Passive and fixed alignment of devices using flexible silicon elements formed by selective etching, J. Micromechan. Microeng., vol. 8, 39-44 (1998)

[4] Martin Hoffmann, Sabine Dickhut, and Edgar Voges, Fiber ribbon alignment structures based on rhombus-shaped channels in silicon, IEEE Photonics Technology Letters, vol. 12, No. 7, (2000)

[5] M. Alavi, S. Buttgenbach, A. Schumacher, and H.-J. Wagner, "Fabrication of microchannels by laser machining and anisotropic etching of silicon," Sensors Actuators, vol. A32, 299-302 (1992)

Micro-grating operating in the 405um spectrum:
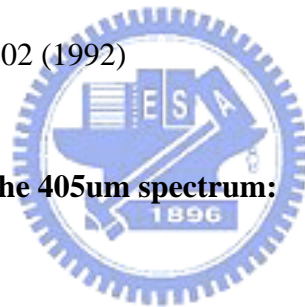
[1] S. S. Lee, L.Y. Lin, and M.C. Wu, Surface-micro-machined free-space micro-optical systems containing three-dimensional micro-gratings, IEEE

[2] L. Y. Lin, S. S. Lee, K. S. J. Pister, M. C. Wu, Micro-machined three-dimensional micro-optics for integrated free-space optical system, IEEE Photonics Technology Letters, Volume: 6, Issue: 12, 1445 – 1447 (1994)

Appendix 1: Remote-controlled Labview codes for the
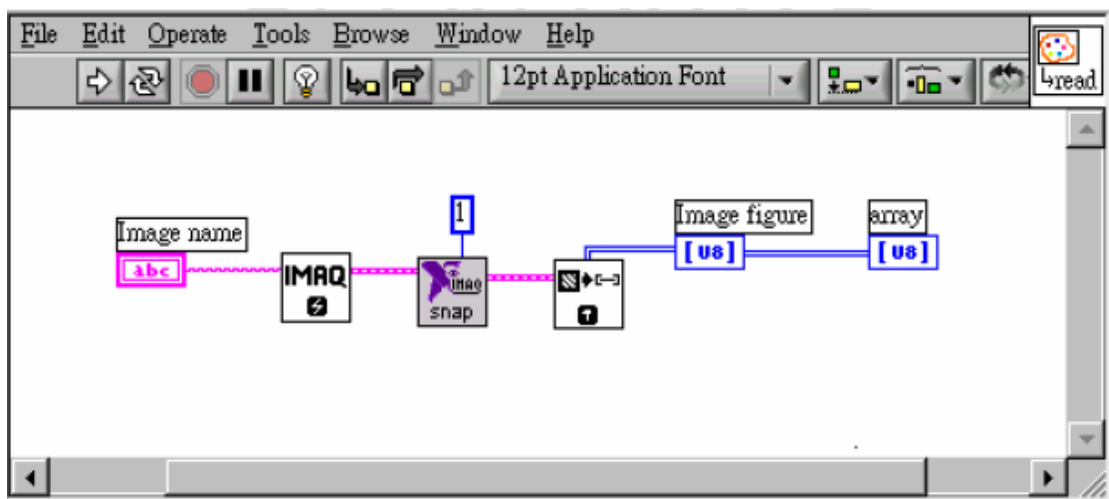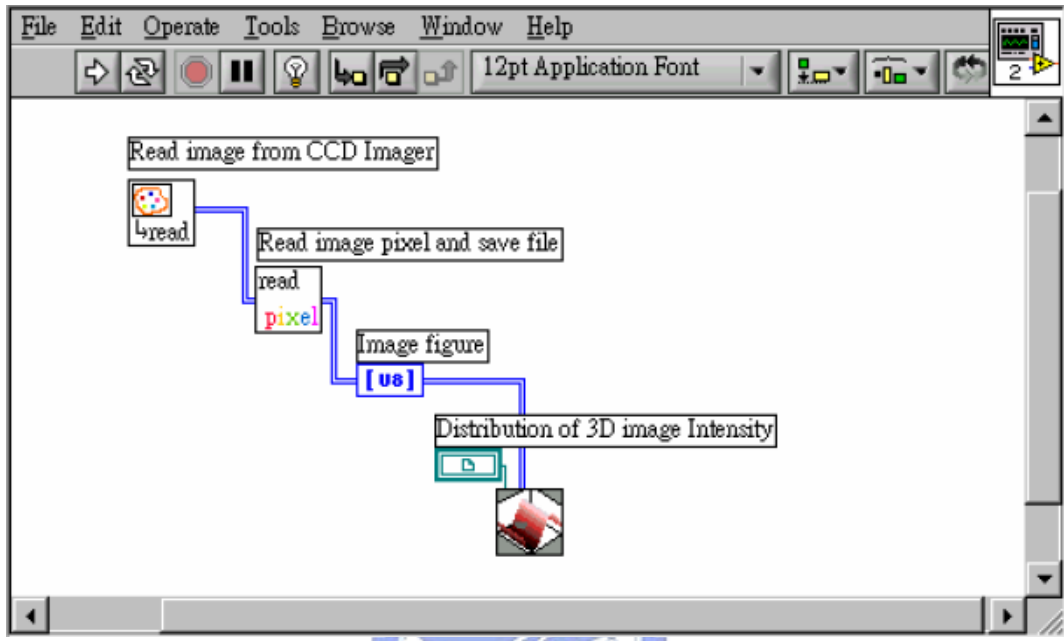
measurement of the spot size

Fig. 1-2 Remote-controlled Labview code for captured image transformed to data array.
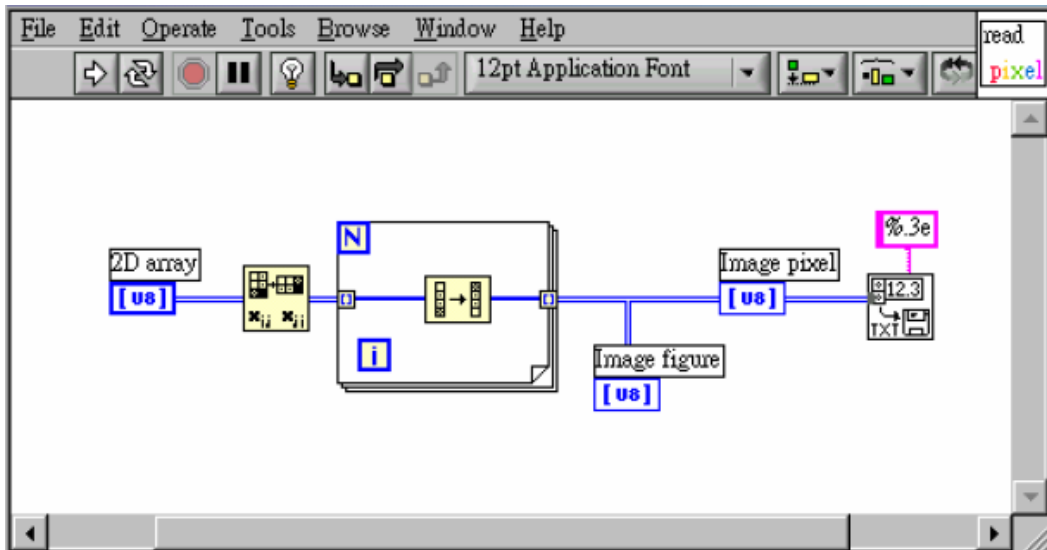
Fig. 1-3 Remote-controlled Labview code for saving the transposed data array.

Appendix 2

This appendix lists some references about Rigorous Coupled Wave Analysis, which is used by GSOLVER.

[1] M. G. Moharam and T. K. Gaylord, "Diffraction Analysis of Dielectric Surface -Relief Gratings", J. Opt. Soc. Am. **72**, 1385 (1982)

[2] T. K. Gaylord and M. G. Moharam, "Analysis and Applications of Optical Diffraction by Gratings", Proc. of the IEEE **73**, 894 (1985)

[3] M. G. Moharam and T. K. Gaylord, "Rigorous coupled-wave analysis of metallic surface-relief gratings", J. Opt. Soc. Am. A **3**, 1780 (1986)

[4] T. K. Gaylord, W. E. Baird and M. G. Moharam, "Zero-reflectivity high spatial-frequency rectangular-grove dielectric surface-relief gratings", Appl. Opt. **25**, 4562 (1986)

[5] L. Li, "Multilayer modal method for diffraction gratings of arbitrary profile, depth, and permittivity", J. Opt. Soc. Am. A **10**, 2581 (1993)

[6] L. Li and C. W. Haggans, "Convergence of the coupled-wave method for metallic lamellar diffraction gratings", J. Opt. Soc. Am. A **10**, 1185 (1993)

[7] E. Popov, L. Tsonev, and D. Maystre, "Lamellar metallic grating anomalies", Appl. Opt. **33**, 5214 (1994)